

Direct numerical simulation of particle-laden and bubble flows

DEREK W. HARRISON

October 10, 2014

Contents

1	Introduction	5
1.1	Background	5
1.2	Thesis objective	7
2	Immersed Boundary method	8
2.1	Introduction	8
2.2	Model equations	8
2.3	Immersed boundary method	9
2.4	Hard-sphere model	12
2.5	Particle advection	12
2.5.1	Rigid body momentum	12
2.5.2	Numerical evaluation of particle momenta	14
3	Front tracking	15
3.1	Introduction	15
3.2	Model equations	16
3.3	Phase fractions	16
3.4	Surface tension force and pressure discontinuity	17
3.5	Front tracking method	18
4	Verification and validation	20
4.1	Verification and validation of Immersed Boundary method	20
4.1.1	Volume integrals vs rigid body	20
4.1.2	Light particle rise velocity	21
4.1.3	Single particle sedimentation	23
4.2	Verification and validation of Front Tracking algorithm	27
4.2.1	Stationary bubble test	27
4.2.2	Standard advection test	27
4.2.3	Oscillating drop	28
4.2.4	Free rise velocity and bubble shape	32
5	Particle-laden and bubbly flows	34
5.1	Particle-laden flows	34
5.2	Bubble flows	40

6	Conclusion	45
7	Recommendations	47

Chapter 1

Introduction

1.1 Background

Particle-laden and bubble flows are encountered in a wide variety of processes in the chemical industry. Some examples are: in flotation devices, in fluidized bed reactors or inverse fluidized bed reactors and bubble columns. Their widespread occurrence has led to considerable interest in understanding the dynamics of these types of flows as such knowledge can be used to optimize the processes in which such flows are encountered.

Studying the dynamics of particle-laden and bubble flows can be done in two ways, experimentally or numerically via simulation of mathematical models. Experimental methods are the most common methods of research and the research done so far has provided much insight into the dynamics of particulate flows. With current state of the art techniques such as particle tracking velocimetry (PTV), particle image velocimetry (PIV) one can obtain relatively detailed information on the flow system being studied. However when the flow pattern becomes relatively complex such techniques can fail to resolve the flow pattern in detail thus preventing comprehensive understanding of the flow behaviour. Other techniques involving probes, like hot wire anemometry, are inadequate for comprehensive studies of complex flows as they alter the flow pattern. In some cases it may not even be possible to study the flow pattern experimentally due to hazardous or extreme conditions (e.g.: high temperatures or corrosive chemicals). In such cases numerical analysis of flow models can provide information on flow behaviour.

Application of numerical methods for simulation of particle-laden and bubble flows has, until recently, been limited to equations of motion of relatively simple systems (such as the motion of single particles or bubbles in a liquid in 2D) or phenomenological models due to limitations in computer processing power. These limitations are now diminishing as computer processing power increases, which doubles roughly every 18 months. Currently processing power has reached the point that even complex flow patterns can be studied numerically. This

has led to and upsurge of application of numerical methods for studies on flow systems which has led to a corresponding upsurge in the development of efficient numerical methods for solving flow governing equations.

There are several advantages of numerical methods over experimental methods. One is that it avoids the costs associated with experimental studies of flow systems. Another is that where flow systems cannot be studied experimentally, due to hazardous or extreme conditions in the flow system, numerical methods can be applied. Finally the results obtained from numerical studies can provide full detail on the flow pattern. It therefore becomes attractive to apply numerical methods for studying a variety of complex flow patterns.

In principle, any type of flow can be simulated numerically with the currently available numerical methods, however processing power (though significantly greater than a decade ago) has not yet reached the point where fully resolved flow simulations of industrial scale processes (typically with dimensions in the order of tens of meters) is feasible due to the large computation time required for a resolved solution of the governing flow equations. Yet it is important to be able to simulate such large scale systems. To overcome this issue (Deen, 2004) have developed a multiscale modeling strategy. The one drawback of the strategy is reduced resolution of fluid flow, however it is a compromise which inevitably must be made. In the multiscale modeling strategy simulations of large scale systems is achieved by deriving closures from fully resolved simulations of flows at small scales (with dimensions in the order of millimeters). At these scales direct numerical simulations are performed (DNS), based on unsimplified equations of motion.

The main focus of this work lies in fully resolved small scale simulations of the particle-laden and bubble flows, i.e.: flows of particles with rigid and mobile surfaces, respectively, in liquids. There are various numerical methods available for simulating these types of flows. In this work it has been chosen to work with an immersed boundary method (IB) for particle-laden flows and a front tracking (FT) method for bubble flows.

The IB method is a method originally devised by Peskin (1971) for simulation of fluid flow around heart valves. This method has proved useful for simulating flows which interact with solid surfaces. Based on this method Uhlmann (2005) devised a numerical method for simulation of particle-laden flows and performed simulations of sedimentation of circular disks, single particles and collections of particles. The ideas of Uhlmann (2005) were then closely followed by Kriebitzsch (2011) who also developed an IB method for simulating particle-laden flows and performed simulations of fluid flow around cylindrical particles and small scale fluidized systems. However, the IB methods used by Uhlmann (2005) and Kriebitzsch (2011) are constrained to simulations of systems where the particle (mass) density is at least 20 % greater than the continuous liquid phase density. This is due to the manner in which the particle momenta are determined. In these methods particle momenta are calculated using a rigid body assumption which leads to a singularity in the equations of motion of particles when the density of the particles is equal to that of the surrounding liquid phase. The singularity renders the schemes unstable at lower ratios of the particle density

to liquid density. Later Kempe (2012) resolved this issue by calculating the particle momenta using volume integrals, thereby avoiding the introduction of a singularity in the equation of motion of particles.

Front tracking is a method devised by Tryggvason (1992) for simulation of multi-fluid flows with sharp interfaces. The method been used to simulate, among other things, the motion of bubbles in a liquid, e.g.: Tryggvason (1992), Tryggvason (2001) and van Sint Annaland (2006). Front tracking has also been applied to study the dynamics of bubble swarms in liquids in the work of Roghair (2012).

1.2 Thesis objective

The main objective of this thesis is to incorporate the method proposed by (Kempe, 2012) for calculating particle momenta into the IB method developed by Kriebitzsch (2011). Once incorporated simulations of particle-laden flows at various solids densities and fractions will be performed to study the effect of particle density and solids fraction on the drag force exerted on the particles by the liquid. Also the effect of surface mobility on particle drag will be studied, by comparing particle-laden simulations with corresponding bubble flow simulations. The objectives in summary fashion:

- Implement a numerical technique for calculating particle momenta in the IB method developed by Kriebitzsch (2011).
- Study the effect of particle density and solids fraction in particle-laden flows.
- Study the effect of surface mobility on drag.

Chapter 2

Immersed Boundary method

2.1 Introduction

Simulations of particle-laden flow systems are carried out using an immersed boundary method (IB) developed by Kriebitzsch (2011) in which the method proposed by Kempe (2012) for calculating particle momenta is incorporated. The IB method is an Euler-Lagrange technique where variables such as pressure and fluid velocity are calculated on a fixed cartesian grid and solid-liquid interface locations are tracked explicitly by Lagrangian meshes. The solid-liquid particle interface is tracked using forcing points which are evenly distributed over the interface with positions fixed with respect to the position of the particle's center. A finite volume is attributed to each of the force points. Interaction between liquid and particle is taken into account via interaction equations involving Dirac delta distribution functions which are used to distribute certain values from the force points to the fixed cartesian grid and vice versa. The most attractive aspect of this Euler-Lagrange technique is the fact that grid generation is relatively straightforward. It is a method by which complicated schemes involving body conforming grids is circumvented, yet retains the advantage of such schemes regarding accurate tracking of interface locations.

2.2 Model equations

The dynamic motion of fluids in particle-laden flows is modeled by the the Navier-Stokes equation:

$$\rho \frac{\partial \mathbf{u}}{\partial t} + \rho \nabla \cdot \mathbf{u} \mathbf{u} = - \nabla p + \rho \mathbf{g} - \nabla \cdot \boldsymbol{\tau} + \mathbf{f}^{IB} \quad (2.1)$$

where \mathbf{u} is the local fluid velocity, \mathbf{g} the gravitational acceleration, $\boldsymbol{\tau}$ the stress tensor, p the local pressure, ρ the local density of the fluid phase and t the time. The solids-fluid interaction is taken into account via the immersed

boundary force term \mathbf{f}^{IB} defined in such a way that the no slip condition at the solid-fluid interface is satisfied. The system must satisfy mass continuity:

$$\nabla \cdot \rho \mathbf{u} = 0 \quad (2.2)$$

Dynamic motion of particles in fluids is governed by Newton's second law and conservation of angular momentum. Application of Newton's second law provides a relation for the translational velocity \mathbf{v}_i of particle i :

$$m_{p,i} \frac{d\mathbf{v}_i}{dt} = (\rho_s - \rho_f) V_{p,i} \mathbf{g} + \mathbf{F}_{f \rightarrow s,i} + \sum_{j \neq i} \mathbf{F}_{c,j \rightarrow i} \quad (2.3)$$

where $\mathbf{F}_{f \rightarrow s,i}$ is the hydrodynamic force, $\mathbf{F}_{c,j \rightarrow i}$ the force exerted on particle i by collision with neighboring particle j , ρ_s is the density of the solids, ρ_f is the density of the liquid phase, $V_{p,i}$ the volume of particle i and $m_{p,i}$ is the mass of particle i . The hydrodynamic force exerted on particle i by the surrounding liquid is given by the surface integral of shear forces normal to the solid-liquid interface over the surface of the solid-liquid boundary:

$$\mathbf{F}_{f \rightarrow s,i} = -\rho_f \oint_S \boldsymbol{\tau} \cdot \mathbf{n} dS \quad (2.4)$$

with \mathbf{n} the unit vector normal to the solid-liquid boundary and S is the surface area of the solid-liquid boundary. From conservation of angular momentum the following relation for the angular velocity $\boldsymbol{\omega}_i$ of particle i is obtained:

$$\Theta_{p,i} \frac{d\boldsymbol{\omega}_i}{dt} = \mathbf{T}_{f \rightarrow s,i} + \sum_{j \neq i} \mathbf{T}_{c,j \rightarrow i} \quad (2.5)$$

where $\Theta_{p,i}$ is the moment of inertia for spherical particles, $\boldsymbol{\omega}_i$ the angular velocity of particle i , $\mathbf{T}_{f \rightarrow s,i}$ the hydrodynamic torque and $\mathbf{T}_{c,j \rightarrow i}$ the collision torque. The hydrodynamic torque on particle i is given by the surface integral of the local torque at surface element dS due to shear stresses over the surface of the solid-liquid boundary:

$$\mathbf{T}_{f \rightarrow s,i} = - \oint_S (\mathbf{x} - \mathbf{r}_i) \times (\boldsymbol{\tau} \cdot \mathbf{n}) dS \quad (2.6)$$

where \mathbf{x} is the position vector of a point on the solid-liquid interface relative to the domain origin and \mathbf{r}_i is the position vector of the center of mass of particle i relative to the domain origin.

2.3 Immersed boundary method

Solution of the model equations begins with the calculation of the immersed boundary force \mathbf{f}^{IB} . The immersed boundary force is used to impose the no-slip

condition at the solid-liquid interface. Calculation of the immersed boundary force is done iteratively. The procedure begins with the estimation of an intermediate velocity field $\hat{\mathbf{u}}^0$ using the information from the previous time step n :

$$\hat{\mathbf{u}}^* = \mathbf{u}^n + \frac{\Delta t}{\rho} (-\nabla p - \rho \nabla \cdot \mathbf{u}\mathbf{u} - \nabla \cdot \boldsymbol{\tau}_e + \rho \mathbf{g})^n \quad (2.7)$$

where n is the old time step. Equations are solved on a staggered Cartesian grid using a fractional step method. Part of the diffusion terms in the stress tensor are treated implicitly following Uhlmann (2005). This partial treatment of the diffusion terms decouples the linear system which must be solved for each velocity component. The explicit part of the stress tensor $\boldsymbol{\tau}_e$ is given by:

$$\boldsymbol{\tau}_e^n = \begin{bmatrix} 0 & -\eta \frac{\partial u_x^n}{\partial y} & -\eta \frac{\partial u_x^n}{\partial z} \\ -\eta \frac{\partial u_y^n}{\partial x} & 0 & -\eta \frac{\partial u_y^n}{\partial z} \\ -\eta \frac{\partial u_z^n}{\partial x} & -\eta \frac{\partial u_z^n}{\partial y} & 0 \end{bmatrix} \quad (2.8)$$

The convective transport term is discretized using a second-order flux-limited Barton scheme (Centralla, 1984) whereas the diffusion terms are discretized using a second order central differencing scheme. The intermediate velocity field $\hat{\mathbf{u}}$ is then obtained by solving:

$$\hat{\mathbf{u}} = \hat{\mathbf{u}}^* - \frac{\Delta t}{\rho} \nabla \cdot \hat{\boldsymbol{\tau}}_i \quad (2.9)$$

with $\hat{\boldsymbol{\tau}}_i$ the (fully time) implicit part of the stress tensor:

$$\hat{\boldsymbol{\tau}}_i = \begin{bmatrix} -2\eta \frac{\partial \hat{u}_x}{\partial x} & -\eta \frac{\partial \hat{u}_y}{\partial x} & -\eta \frac{\partial \hat{u}_z}{\partial x} \\ -\eta \frac{\partial \hat{u}_x}{\partial y} & -2\eta \frac{\partial \hat{u}_y}{\partial y} & -\eta \frac{\partial \hat{u}_z}{\partial y} \\ -\eta \frac{\partial \hat{u}_x}{\partial z} & -\eta \frac{\partial \hat{u}_y}{\partial z} & -2\eta \frac{\partial \hat{u}_z}{\partial z} \end{bmatrix} \quad (2.10)$$

Estimation of the intermediate velocity is followed by an estimate of the tentative velocity $\hat{\mathbf{U}}_m^p$ at force point with position \mathbf{X}_m via interpolation of the velocities at the Eulerian grid cells surrounding the force point to the force point using the following equation:

$$\hat{\mathbf{U}}_m^p = \sum_{i,j,k} D \left(\frac{\mathbf{x}_i - \mathbf{X}_m}{h} \right) \hat{\mathbf{u}}_{i,j,k}^p \quad (2.11)$$

where \mathbf{x}_i is the position vector of the Eulerian grid cells surrounding the Lagrangian force points, $\hat{\mathbf{u}}_{i,j,k}^p$ is the intermediate velocity vector a cell (i,j,k) , h

the grid size, p the iteration counter and D the fourth order cheap clipped polynomial of Deen (2004). Next the actual velocity at a marker point is calculated using the known angular and translational velocities of the particle:

$$\mathbf{V}_m = \mathbf{v}_i + \boldsymbol{\omega}_i \times (\mathbf{X}_m - \mathbf{r}_i) \quad (2.12)$$

where \mathbf{V}_m is the actual velocity of the marker point. With the actual velocity of the marker point and the first estimate for the tentative velocity known, a first estimate of the immersed boundary force at a marker point \mathbf{F}_m^{IB} can be obtained:

$$\mathbf{F}_m^{IB,p+1} = \mathbf{F}_m^{IB,p} + \frac{\rho_f}{\Delta t} (\mathbf{V}_m - \hat{\mathbf{U}}_m^p) \quad (2.13)$$

At iteration count $p = 0$ the immersed boundary force is equal to zero. With the immersed boundary force at a force point estimated, the immersed boundary force at Eulerian grid cells is calculated by mapping the immersed boundary force onto the Eulerian grid:

$$\mathbf{f}_{i,j,k}^{IB,p+1} = \sum_m D \left(\frac{\mathbf{x}_{i,j,k} - \mathbf{X}_m}{h} \right) \mathbf{F}_m^{IB,p+1} \frac{\Delta V_m}{h^3} \quad (2.14)$$

With the immersed boundary force calculated at the Eulerian grid cells the velocity field $\hat{\mathbf{u}}^{p+1}$ is calculated by solving equation 2.7 with the immersed boundary force included:

$$\hat{\mathbf{u}}^{*,p+1} = \mathbf{u}^n + \frac{\Delta t}{\rho} (-\nabla p - \rho \nabla \cdot \mathbf{u} \mathbf{u} - \nabla \cdot \boldsymbol{\tau}_e + \rho \mathbf{g} + \mathbf{f}^{IB,p+1})^n \quad (2.15)$$

and subsequently:

$$\hat{\mathbf{u}}^{p+1} = \hat{\mathbf{u}}^{*,p+1} - \frac{\Delta t}{\rho} \nabla \cdot \hat{\boldsymbol{\tau}}_i$$

The new estimate of the velocity field $\hat{\mathbf{u}}^{p+1}$ is used to re-estimate the tentative velocity at the force points. If the estimated tentative velocities and actual particle velocities differ by no more than some predefined amount than the iteration is stopped and the intermediate velocity field $\hat{\mathbf{u}}^{p+1}$ should satisfy the no slip condition at the solid-liquid interface. If not the calculations are repeated starting from equation 2.11 using the most recent estimate of the velocity field, $\hat{\mathbf{u}}^{p+1}$.

Once the intermediate field $\hat{\mathbf{u}}^{p+1}$ satisfies the no-slip condition mass continuity is imposed by first obtaining the local pressure correction ϕ :

$$\nabla^2 \phi^{n+1} = \frac{\rho_f}{\Delta t} \nabla \cdot \hat{\mathbf{u}}^{p+1} \quad (2.16)$$

then correcting the intermediate velocity and pressure field:

$$\mathbf{u}^{n+1} = \hat{\mathbf{u}}^{p+1} - \frac{\Delta t}{\rho_f} \nabla \phi^{n+1} \quad (2.17)$$

$$p^{n+1} = p^n + \phi^{n+1} \quad (2.18)$$

obtaining the velocity and pressure fields at the next time step.

Finally, the positions and velocities of the particles are updated using the discretized form of equations 2.3 and 2.5.

2.4 Hard-sphere model

The hard-sphere model is a model for particle collisions. In this model it is assumed that collisions are instantaneous, consequently only binary collisions occur which is a realistic assumption for dilute systems. The translational and angular velocities of the particle after collisions are deduced from conservation of momentum principles. The model takes possible slip between the particles into account, which occurs when the relative velocities of the particles are of sufficient magnitude, via friction coefficients (Hoomans, 1996). If the friction force between two particles during collision exceeds the friction coefficient then slip occurs. Energy dissipation is taken into account via restitution coefficients. Although in this work only ideal collisions are considered.

The main parameter in the hard-sphere model is the collision time. The collision-time is the time at which the following collision between any two particles in a multi-particle system will occur:

$$t_{ab} = \frac{-\mathbf{r}_{ab} \cdot \mathbf{u}_{ab} - \sqrt{(\mathbf{r}_{ab} \cdot \mathbf{u}_{ab})^2 - \mathbf{u}_{ab}^2 (\mathbf{r}_{ab}^2 - (R_a + R_b)^2)}}{\mathbf{u}_{ab}^2} \quad (2.19)$$

Here t_{ab} is the collision-time, \mathbf{r}_{ab} is the difference vector between the position vectors of the particles taking place in the following collision, a and b , \mathbf{u}_{ab} is the relative velocity vector and R_a and R_b are the particle radii. This is an important parameter as this time may be lower than the defined time-step (simulation setting) used in simulations. If the collision time is smaller than the defined time-step the particles are advected with a time-step equal to the collision time.

2.5 Particle advection

2.5.1 Rigid body momentum

Advection of the solid particles requires solving the equations of motion of particles, given by equations 2.3 and 2.5. Solution of these equations requires calculation of the hydrodynamic force and torque terms in equation 2.3 and 2.5, respectively. The momentum terms in these equations are calculated by volume integrals, following Kempe (2012). However here the method followed by (Kriebietzsch, 2011) based on the IB method devised by (Uhlmann, 2005) for

simulating particulate flows is given to point out the issue which comes about as a consequence of incorporating the momentum equations for a rigid body in the equations of motion for particles. In Uhlmann (2005) the hydrodynamic force is given by:

$$\mathbf{F}_{f \rightarrow s, i} = -\rho_f \sum_m \mathbf{F}_m^{IB} \Delta V_m + \frac{d}{dt} \int_{V_{p, i}} \rho_l \mathbf{u} dV \quad (2.20)$$

where rate of change in momentum of the particle, represented by the second term on the right-hand side of equation 2.20 is equal to the rate of change in momentum of a corresponding rigid spherical body:

$$\frac{d}{dt} \int_{V_{p, i}} \rho_f \mathbf{u} dV = \rho_f V_{p, i} \frac{d\mathbf{v}_i}{dt} \quad (2.21)$$

Substitution of the above relation into equation 2.20 results in the following relation for the hydrodynamic force term:

$$\mathbf{F}_{f \rightarrow s, i} = -\rho_f \sum_m \mathbf{F}_m^{IB} \Delta V_m + \rho_f V_{p, i} \frac{d\mathbf{v}_i}{dt} \quad (2.22)$$

Combining equations 2.22 and 2.3 gives, after some rearrangement, the following relation for the translational velocity:

$$(\rho_s - \rho_f) V_{p, i} \frac{d\mathbf{v}_i}{dt} = (\rho_s - \rho_f) V_{p, i} \mathbf{g} - \rho_f \sum_m \mathbf{F}_m^{IB} \Delta V_m + \sum_{j \neq i} \mathbf{F}_{c, j \rightarrow i} \quad (2.23)$$

Evaluation of the hydrodynamic torque term is done in a similar manner, resulting in the following equation for the angular velocity:

$$(\rho_s - \rho_f) \frac{\Theta_{p, i}}{\rho_s} \frac{d\boldsymbol{\omega}_i}{dt} = -\rho_f \sum_m (\mathbf{X}_m - \mathbf{r}_i) \times \mathbf{F}_m^{IB} \Delta V_m + \sum_{j \neq i} \mathbf{T}_{c, j \rightarrow i} \quad (2.24)$$

Equations 2.23 and 2.24 are discretized in time by explicit Euler discretization, resulting in:

$$\mathbf{v}_i^{n+1} = \mathbf{v}_i^n + \Delta t \left(\mathbf{g} - \frac{\rho_f}{(\rho_s - \rho_f) V_{p, i}} \sum_m \mathbf{F}_m^{IB} \Delta V_m \right) \quad (2.25)$$

$$\boldsymbol{\omega}_i^{n+1} = \boldsymbol{\omega}_i^n - \Delta t \left(\frac{\rho_f \rho_s}{(\rho_s - \rho_f) \Theta_{p, i}} \sum_m (\mathbf{X}_m - \mathbf{r}_i) \times \mathbf{F}_m^{IB} \Delta V_m \right) \quad (2.26)$$

Note the appearance of a singularity in equation 2.26. The singularity renders the scheme unstable for low particle density to liquid density ratios. Introduction of a singularity can be avoided via numerical evaluation of the volume integral in equation 2.20, thereby increasing the range of particle densities which can be simulated.

2.5.2 Numerical evaluation of particle momenta

In the method outlined by Kempe (2012) calculation of particle momenta is done by evaluating the volume integrals in equations 2.22 and 2.24 numerically. The momentum of a particle is evaluated with:

$$\int_{V_{p,i}} \rho_f \mathbf{u} dV = \sum_i^{N_x} \sum_j^{N_y} \sum_k^{N_z} \rho_f \mathbf{u}_{i,j,k} h^3 \alpha_{i,j,k} \quad (2.27)$$

where α is the volume fraction of solids in each cell. The local volume fraction is calculated using the signed-distance level set function proposed by Kempe (2012). Equation 2.27 is then substituted into the equation for the hydrodynamic force. The equation for the translational velocity of the particle becomes:

$$\rho_s V_{p,i} \frac{d\mathbf{v}_i}{dt} = (\rho_s - \rho_l) V_{p,i} \mathbf{g} + \rho_f \sum_m \mathbf{F}_m^{IB} \triangle V_m + \frac{d}{dt} \sum_i^{N_x} \sum_j^{N_y} \sum_k^{N_z} \rho_f \mathbf{u}_{i,j,k} h^3 \alpha_{i,j,k} \quad (2.28)$$

The angular momentum of the (fluid within the) particle is evaluated with:

$$\rho_f \int_{V_{p,i}} \mathbf{r} \times \mathbf{u} dV = \sum_i^{N_x} \sum_j^{N_y} \sum_k^{N_z} \rho_f \mathbf{r}_{i,j,k} \times \mathbf{u}_{i,j,k} h^3 \alpha_{i,j,k} \quad (2.29)$$

This equation is then substituted into the equation for the hydrodynamic torque:

$$\Theta_{p,i} \frac{d\boldsymbol{\omega}_i}{dt} = -\rho_f \sum_m (\mathbf{X}_m - \mathbf{r}_i) \times \mathbf{F}_m^{IB} \triangle V_m + \frac{d}{dt} \sum_i^{N_x} \sum_j^{N_y} \sum_k^{N_z} \rho_f \mathbf{r}_{i,j,k} \times \mathbf{u}_{i,j,k} h^3 \alpha_{i,j,k} \quad (2.30)$$

In this method no singularity is present, making it possible to simulate particles with densities equal to and lower than the surrounding fluid. This method has been incorporated into the current IB method, developed by (Kriebitzsch, 2011), increasing the range of particle densities which can be simulated.

Chapter 3

Front tracking

3.1 Introduction

A variety of different methods exist which are able to account for gas-liquid interactions. Some examples of such techniques are level set methods, volume of fluid methods and marker particle methods. These differ in the manner in which interfaces are tracked and advected and how local phase fractions are determined (an important parameter in the model equations).

Advantages of the level set methods, which tracks the gas-liquid interface by solving the zero level set of a distance function (Sussman, 1994), are its conceptual simplicity and consequently its straightforward implementation in a code. The downside is limited accuracy and volume conservation.

In volume of fluid methods the interface is tracked using local phase fractions. Advantages of this method are its conceptual simplicity, the ability to account for substantial interface deformations. The downside is artificial coalescence and break-up of disperse phase elements.

Marker particle methods are highly accurate, robust and are able to account for substantial interface deformations. Unfortunately these methods come at a high computational cost.

None of the disadvantages mentioned in these three methods are present in current FT methods. Which makes the use of FT methods attractive. Another aspect which makes FT attractive is the accuracy with which the interface is tracked together with interface resolution. This enables one to accurately account for interfacial pressure drop and interfacial forces which reduces spurious currents from forming at the interface. However the use of interaction equations and Dirac delta functions is generally regarded as a drawback. Another drawback is the need for interfacial grid remeshing techniques to ensure mass conservation of the dispersed phase is satisfied. These advantages FT methods are the reasons this method was chosen for simulation of bubbly flows.

3.2 Model equations

The dynamic motion fluids in bubble flow systems are modeled by the Navier-Stokes equation:

$$\rho \frac{\partial \mathbf{u}}{\partial t} + \rho \nabla \cdot \mathbf{u} \mathbf{u} = -\nabla p + \rho \mathbf{g} - \nabla \cdot \boldsymbol{\tau} + \mathbf{f}_\sigma \quad (3.1)$$

where \mathbf{u} is the velocity vector, \mathbf{g} the gravitational acceleration vector, $\boldsymbol{\tau}$ the stress tensor, p the local pressure, ρ the local density of the fluid phase (including both gas and liquid phases, not solids) and t the time. Note that a discontinuity in density and viscosity exists at the gas-liquid interface as in general these properties are not equal for both phases. The gas-liquid interaction is taken into account via the surface tension force density \mathbf{f}_σ . The system must satisfy mass continuity:

$$\nabla \cdot \rho \mathbf{u} = 0 \quad (3.2)$$

The pressure and shear stress discontinuities at the gas-liquid interface. These discontinuities are a consequence of gas-liquid interfacial tension and discontinuities in physical properties (density and viscosity). A relation for these discontinuities can be obtained from a local force balance at the interface between the pressure force, shear stress force and surface tension force:

$$[-p\mathbf{I} - \boldsymbol{\tau}] \cdot \mathbf{n} = \mathbf{F}_\sigma \cdot \mathbf{n} \quad (3.3)$$

At the interface the local normal pressure force, normal shear stress force and surface tension force \mathbf{F}_σ are in mechanical equilibrium. Equation 3.3 also determines the shape of the gas-liquid interface, i.e. the shape of a gas bubble.

3.3 Phase fractions

The one fluid-formulation applied in this requires calculation of the local dispersed phase fractions for determination of the dispersed phase density and viscosity distributions, which are needed for solving the Navier-Stokes equations. Traditionally, a Poisson equation was solved to determine the local dispersed phase fractions in each Eulerian cell, however in this work the phase fractions are calculated using the Lagrangian markers representing the gas-liquid interface.

Calculation of the phase fractions is done by summing up the volumes above or below a marker, depending on the sign of the z-component of the unit vector normal to the marker, in a unit grid cell. Markers occupying more than one grid cell are cut into three smaller triangles in such a way that the markers constitute a plane which fit perfectly in the domain of a grid cell. The location and surface area of the markers are used to determine the volume under a marker:

$$V_m(i, j, k) = \begin{cases} -\mathbf{e}_z \cdot \mathbf{n}_m S_m (k\Delta z - z_m) & k = k_m \\ -\mathbf{e}_z \cdot \mathbf{n}_m S_m \Delta z & k > k_m \end{cases} \quad (3.4)$$

where \mathbf{e}_z is the unit vector in the z-direction, \mathbf{n}_m is the unit vector normal to the marker, S_m is the surface area of a marker in the cell, k is the z-location of the cell, k_m is the height of the Eulerian grid cells (in grid cells with respect to the xy-plane) containing markers with normals with negative z-components, z_m the absolute height of the marker and V_m the volume above (or below) the marker in cell (i, j, k) . Summing up all the volumes corresponding with the gas phase and dividing by the cell volume gives the local gas phase fraction F_g :

$$F_g(i, j, k) = \frac{1}{\Delta x \Delta y \Delta z} \sum_{m \in g} V_m(i, j, k) \quad (3.5)$$

With the phase fraction of phase p known at every cell the local averaged density and viscosity at every cell can be determined. The local average density is determined via a standard volume weighing method:

$$\rho(i, j, k) = F_g(i, j, k) \rho_g + (1 - F_g(i, j, k)) \rho_l \quad (3.6)$$

The local viscosity, however, is determined via harmonic averaging:

$$\frac{\rho(i, j, k)}{\eta(i, j, k)} = F_g(i, j, k) \frac{\rho_g}{\eta_g} + (1 - F_g(i, j, k)) \frac{\rho_l}{\eta_l} \quad (3.7)$$

where η_l is the viscosity of the liquid phase, η_g is the viscosity of the gas phase and F_g is the fraction of gas present in an Eulerian cell. Harmonic averaging is applied as it has been shown that it significantly improves the continuity of tangential stress across the interface. (Prosperetti, 2002)

3.4 Surface tension force and pressure discontinuity

To take into account the surface tension force at the gas-liquid interface a surface tension force source term was introduced into the momentum balance (equation 2.1). Calculation of the the surface tension force at an Eulerian grid cell begins with the calculation of the surface tension force at a Lagrangian marker $\mathbf{F}_{\sigma, m}$. The surface tension force at a Lagrangian marker is then distributed to the Eulerian grid using a mass-weighing distribution function (Deen, 2004).

The surface tension force at a Lagrangian marker is calculated by summing the forces exerted on marker m by its surrounding neighbors i by surface tension:

$$\mathbf{F}_{\sigma, m} = \frac{1}{2} \sum_{i=a, b, c} \mathbf{F}_{\sigma, i \rightarrow m} \quad (3.8)$$

where $\mathbf{F}_{\sigma, i \rightarrow m}$ is the surface tension force neighbor i exerts on marker m with neighbors a , b and c . The surface tension force exerted by neighboring marker i on marker m can be calculated via the following equation:

$$\mathbf{F}_{\sigma, i \rightarrow m} = \sigma (\mathbf{t}_{mi} \times \mathbf{n}_i) \quad (3.9)$$

where \mathbf{t}_{mi} is a vector tangent to a side of marker triangle i and \mathbf{n}_i is the unit vector normal to marker i . With the surface tension force at a marker calculated, the force is distributed to the Eulerian grid :

$$\mathbf{f}_{\sigma,i,j,k} = \frac{\sum_m \rho(i,j,k) D(\mathbf{x}_{i,j,k} - \mathbf{x}_m) \mathbf{F}_{\sigma,m}}{\sum_m \rho(i,j,k) D(\mathbf{x}_{i,j,k} - \mathbf{x}_m)} \quad (3.10)$$

where $\mathbf{x}_{i,j,k}$ is the position vector of Eulerian cell (i,j,k) relative to the origin of the domain, \mathbf{x}_m is the position vector of the marker relative to the origin and $\mathbf{f}_{\sigma,i,j,k}$ is the surface tension at the marker and D the mass-weighting distribution function of Deen (2004):

$$D(\mathbf{r}) = d_x(r_x) d_y(r_y) d_z(r_z) \\ d_\alpha = \begin{cases} 1 - \frac{|r_\alpha|}{h} & |r_\alpha| \leq h \\ 0 & |r_\alpha| > h \end{cases} \quad (3.11) \\ \alpha = x, y, z$$

with h the Eulerian grid spacing, \mathbf{r} an arbitrary vector and d_α a function defined by equation 3.11. Finally, the pressure drop across the gas-liquid interface is calculated by:

$$[p] = \frac{\sum_m (\mathbf{F}_{\sigma,m} \cdot \mathbf{n})}{\sum_m S_m} \quad (3.12)$$

3.5 Front tracking method

The FT method starts of with the determination of the phase fractions. Next the density and viscosity fields are calculated followed by the calculation of the surface tension force. The surface tension force is then used in the following equation to obtain a first estimate of the velocity field \mathbf{u}^{n*} at the following time step:

$$\hat{\mathbf{u}}^* = \mathbf{u}^n + \frac{\Delta t}{\rho} (-\nabla p - \rho \nabla \cdot \mathbf{u} \mathbf{u} - \nabla \cdot \boldsymbol{\tau}_e + \rho \mathbf{g} + \mathbf{f}_\sigma)^n \quad (3.13)$$

where n is the old time step and $\boldsymbol{\tau}_e$ is the explicit part of the stress tensor:

$$\boldsymbol{\tau}_e^n = \begin{bmatrix} 0 & -\eta \frac{\partial u_x^n}{\partial y} & -\eta \frac{\partial u_x^n}{\partial z} \\ -\eta \frac{\partial u_y^n}{\partial x} & 0 & -\eta \frac{\partial u_y^n}{\partial z} \\ -\eta \frac{\partial u_z^n}{\partial x} & -\eta \frac{\partial u_z^n}{\partial y} & 0 \end{bmatrix} \quad (3.14)$$

Equations are solved on a staggered Cartesian grid where velocity nodes are located at the faces of gridcells corresponding with pressure nodes. The convective transport term is discretized using the flux limiter Min-Mod scheme and

the diffusive transport term is discretized using a central differencing scheme. Then a intermediate velocity field $\hat{\mathbf{u}}$ is obtained by solving:

$$\hat{\mathbf{u}} = \hat{\mathbf{u}}^* - \frac{\Delta t}{\rho} \nabla \cdot \hat{\boldsymbol{\tau}}_i \quad (3.15)$$

with $\hat{\boldsymbol{\tau}}_i$ the time implicit part of the stress tensor is given by:

$$\hat{\boldsymbol{\tau}}_i = \begin{bmatrix} -2\eta \frac{\partial \hat{u}_x}{\partial x} & -\eta \frac{\partial \hat{u}_y}{\partial x} & -\eta \frac{\partial \hat{u}_z}{\partial x} \\ -\eta \frac{\partial \hat{u}_x}{\partial y} & -2\eta \frac{\partial \hat{u}_y}{\partial y} & -\eta \frac{\partial \hat{u}_z}{\partial y} \\ -\eta \frac{\partial \hat{u}_x}{\partial z} & -\eta \frac{\partial \hat{u}_y}{\partial z} & -2\eta \frac{\partial \hat{u}_z}{\partial z} \end{bmatrix} \quad (3.16)$$

Mass continuity is then imposed by first obtaining the local pressure correction ϕ :

$$\nabla^2 \phi^{n+1} = \frac{\rho_f}{\Delta t} \nabla \cdot \hat{\mathbf{u}} \quad (3.17)$$

then correcting the intermediate velocity and pressure field:

$$\mathbf{u}^{n+1} = \hat{\mathbf{u}} - \frac{\Delta t}{\rho_f} \nabla \phi^{n+1} \quad (3.18)$$

$$p^{n+1} = p^n + \phi^{n+1} \quad (3.19)$$

obtaining the velocity and pressure fields at the next time step. The velocity field at the new time step $n+1$ is then used to advect the bubbles. Bubble interfaces are advected with the local interpolated velocity. A third order spline is used to interpolate velocities to bubble markers (Dijkhuizen, 2008).

Chapter 4

Verification and validation

4.1 Verification and validation of Immersed Boundary method

4.1.1 Volume integrals vs rigid body

Implementation of the numerical scheme outlined by Kempe (2012) for calculating particle momenta is tested by simulating sedimentation of single particles. Single particles are placed at some location in a liquid filled cubic box. They are then released at $t = 0$ and allowed to settle at the bottom of the box.

Simulation settings are given in Table 4.1. Results obtained with the new scheme implemented are compared with the results obtained with the previous scheme used for calculating particle momenta (using rigid body assumptions), which has been verified and validated by Seelen (2012) and Kriebitzsch (2011). The comparison is shown in Figure 4.1. The results agree well with an error less than 1 % between the two schemes, indicating succesful implementation of the new numerical scheme.

Table 4.1: Simulation settings for single particle sedimentation

Computational grid	140 x 140 x 180	—
Grid size	2.5E-05	(<i>m</i>)
Numer of time steps	100000	—
Time step	1.0E-5	(<i>m</i>)
Particle diameter	0.0005	(<i>m</i>)
Initial particle position	(x,y,z) = (0.00175,0.00175,0.001)	(<i>m</i>)
Liquid density	1000	(<i>kg/m</i> ³)
Liquid viscosity	0.00090366	(<i>kg/ms</i>)
Particle density	2560	(<i>kg/m</i> ³)

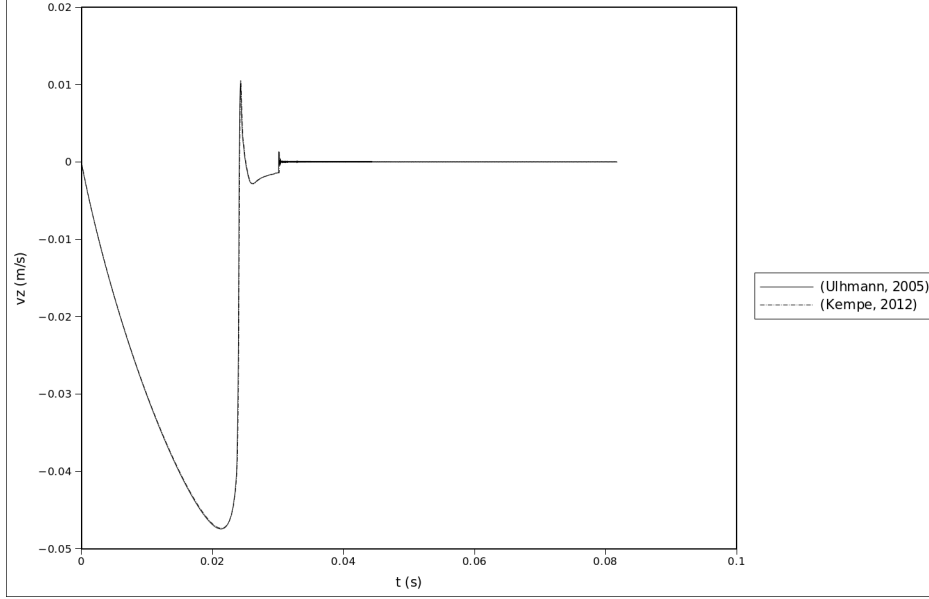


Figure 4.1: Particle settling velocities obtained from simulations with new IB scheme for calculating particle momenta (Kempe, 2012) and previously used scheme (Uhlmann, 2005).

4.1.2 Light particle rise velocity

Simulations of light particles (particles with densities lower than the surrounding liquid phase) rising in an initially quiescent liquid are performed to test the accuracy of IB method with the new scheme implemented, henceforth shortened to new IB method, in predicting particle trajectories under experimental conditions. Single particles are placed in a liquid filled cubic box and released at $t = 0$. Particle velocities obtained with the new IB method are compared with particle velocities obtained by solving the macroscopic force balance for particles:

$$\left(\rho_s + \frac{1}{2}\rho_f\right) V_p \frac{d\mathbf{v}}{dt} = V_p (\rho_p - \rho_f) \mathbf{g} - \frac{1}{8} C_D \rho_f \pi d_p^2 |\mathbf{v} - \mathbf{u}| (\mathbf{v} - \mathbf{u}) \quad (4.1)$$

where \mathbf{v} is the particle velocity and \mathbf{u} the liquid velocity. The virtual mass coefficient is set to 0.5. Two different correlations are used for predicting the rise velocity of particles. The first is the correlation of Turton and Levenspiel (1986):

$$C_D = \frac{24(1 + 0.173Re^{0.657})}{Re} + \frac{0.413}{1 + 16300Re^{-1.09}} \quad (4.2)$$

Table 4.2: Simulation settings for single rising light particle

Computational grid	140 x 140 x 180	—
Grid size	2.5E-05	(<i>m</i>)
Numer of time steps	100000	—
Time step	1.0E-5	(<i>m</i>)
Particle diameter	0.0005	(<i>m</i>)
Initial particle position	(x,y,z) = (0.00175,0.00175,0.0035)	(<i>m</i>)
Liquid density	1000	(<i>kg/m</i> ³)
Liquid viscosity	0.00090366	(<i>kg/ms</i>)
Particle density	500	(<i>kg/m</i> ³)

Table 4.3: Comparison between simulation and correlations

	v_z	Re
Simulation	0.031	16
Turton (1986)	0.033	17
Beetstra (2007)	0.036	18

who arrived at this correlation by fitting a postulated empirical equation to experimental data reported in literature. The second is the correlation of Beetstra (2007) (equation 5.1), the details of which are given in section 5.1. Simulation settings are given in Table 4.2. Simulation results are shown in Figure 4.2. Terminal rise velocity based on the correlation of Turton and Levenspiel (1986) is greater than that obtained from simulation. This is may be due to confinement, an effect which can become significant in simulations where the scale of the simulation domain is relatively small, e.g.: when the characteristic length of the simulation domain is in the same order of magnitude as that of the particle, which is the case in the simulations performed in this work. Experimental techniques for determining rising particle velocities do not usually suffer from such effects as the dimensions of the vessels in which the experiments are carried out are usually an order of magnitude larger than the particle dimensions. However the increased drag observed in simulation may also be a consequence of the use of distribution functions which have been shown to enlarge the particle diameter “felt” by the surrounding fluid (Kriebitzsch, 2011; Tang, 2014). Low particle resolutions (particle diameter / grid size) can also results in overestimation of the drag force (Tang, 2014), but this seems unlikely as a resolution of 20 was used in this work and Kriebitzsch (2011) showed that simulations with higher resolutions do not result in a significant change in simulation results.

Although differences are observed, the relative difference between the terminal rise velocity obtained from simulations and the terminal rise velocity calculated based on the correlation of Turton and Levenspiel (1986) is 6 %. The difference between the IB method and prediction based on Beetstra (2007) is slightly greater at 14 %.

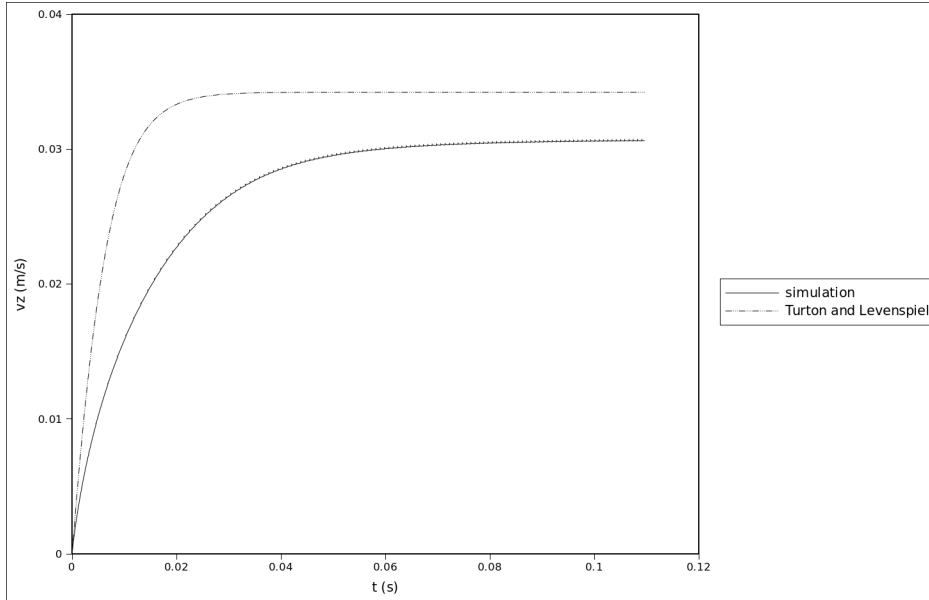


Figure 4.2: Light particle rising in an initially quiescent liquid.

4.1.3 Single particle sedimentation

Single particle sedimentation simulations are performed to test the accuracy of the new IB method in predicting particle trajectories under experimental conditions. Similar to the case where light particles are simulated, only now the particle densities are greater than that of the surrounding liquid. Single particles are placed in a liquid filled cubic box and released at $t = 0$. Again particle trajectories simulated using the new IB method are compared with particle trajectories obtained by solving the macroscopic force balance for particles in combination with the drag force correlation of Turton and Levenspiel (1986) or Beetstra (2007).

Simulation settings are given in Table 4.4 and 4.5. Three different cases are studied. The first case corresponds with case 1 in the experimental work of Mordant (2000). Cases 2 and 3 correspond with cases 2 and 3 in the works Ten Cate (2002). In the simulation representing case 1 in the work of Mordant (2000) the domain size to particle size ratio is far smaller than those used in experiments of Mordant (2000). In contrast, the domain size to particle size ratio used in simulations representing the cases in Ten Cate (2002) is the same as that used in the experiments of Ten Cate (2002).

A plot of the settling velocity obtained from the simulation representing case 1 in the work of Mordant (2000) and prediction based on the correlation of Turton and Levenspiel (1986) is shown in Figure 4.3. The terminal velocity of the particle is compared with the terminal sedimentation velocities observed in case 1 in Mordant (2000) and with predictions based on the correlations of Turton

Table 4.4: Simulation settings for single particle sedimentation

	1	2	
Computational grid	140 x 140 x 180	106 x 106 x 170	—
Grid size	2.5E-05	9.4339623e-4	(<i>m</i>)
Numer of time steps	100000	100000	—
Time step	1.0E-5	1.0E-4	(<i>m</i>)
Particle diameter	0.0005	0.015	(<i>m</i>)
Initial particle position (x,y,z)	(0.00175,0.00175,0.001)	(0.05,0.05,0.12)	(<i>m</i>)
Liquid density	1000	965	(<i>kg/m</i> ³)
Liquid viscosity	0.00090366	0.212	(<i>kg/ms</i>)
Particle density	2560	1120	(<i>kg/m</i> ³)

and Levenspiel (1986) and Beetstra (2007). These results are summarized in Table 4.6. Terminal sedimentation velocities obtained in Mordant (2000) agree reasonably well with predictions based on correlations. Results for case 1 in Mordant (2000) also agrees well with the IB simulation. The relative difference between terminal velocities obtained with the IB method and the work of Mordant (2000) is within 5 %. The difference between simulation and correlation of Turton and Levenspiel (1986) is slightly greater, at 8 %. The increased drag observed in simulations in comparison with predictions based on correlations and the experimental results of Mordant (2000) is possibly due to confinement, but likely due to an enlargement of the particle diameter resulting from the use of distribution functions since increased drag is also observed in the simulation cases which represent the experimental cases of Ten Cate (2002) where simulation settings were set to the exact values used in the experimental cases. Results are summarized in Table 4.6.

Simulation results corresponding with the experimental cases of Ten Cate (2002) are summarized in Table 4.7. A plot of the settling velocity as a function of time is given in Figure 4.4. The settling velocity observed in simulation is slightly lower than that observed in the experimental work of Ten Cate (2002). The simulation settings however exactly represent the experimental conditions (domain size, particle size, physical properties). Therefore one cannot attribute the greater drag observed in simulations to confinement effects. It thus seems likely that the increased drag is a consequence of the distribution functions enlarging particle diameter. Though overall the IB method and results of the experiments of Ten Cate (2002) agree reasonably well, within 8 %.

Table 4.5: Simulation settings for single particle sedimentation

3		
Computational grid	106 x 106 x 170	—
Grid size	9.4339623e-4	(<i>m</i>)
Numer of time steps	100000	—
Time step	1.0E-4	(<i>m</i>)
Particle diameter	0.015	(<i>m</i>)
Initial particle position (x,y,z)	(0.05,0.05,0.12)	(<i>m</i>)
Liquid density	962	(<i>kg/m</i> ³)
Liquid viscosity	0.113	(<i>kg/ms</i>)
Particle density	1120	(<i>kg/m</i> ³)

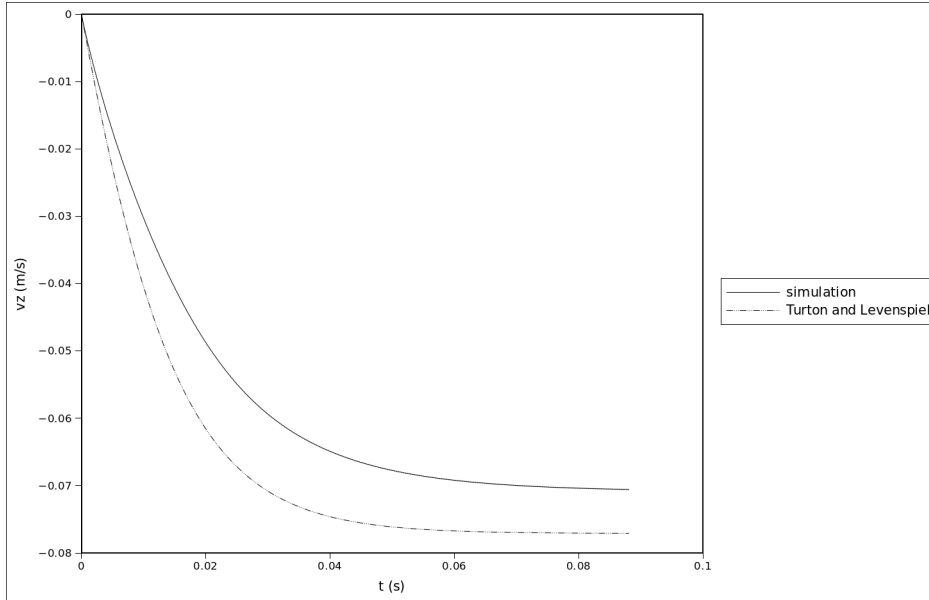


Figure 4.3: Particle sedimentation velocities.

Table 4.6: Comparison of simulation results with case 2 and 3 of the experimental studies performed by Mordant (2000) and predictions based on the correlation of Beetstra (2007) and Turton and Levenspiel (1986).

	v_z	Re
Simulation	0.071	39
Turton (1986)	0.077	43
Beetstra (2007)	0.076	41
Mordant (2000)	0.074	41

Table 4.7: Comparison of simulation results with case 2 and 3 of the experimental studies performed by Ten Cate (2002) and predictions based on correlations of Beetstra (2007) and Turton and Levenspiel (1986).

Case	Re Simulation	Re Ten Cate (2002)	Re Beetstra (2007)	Re Turton (1986)
2	3.8	4.1	4.1	4.2
3	10.7	11.6	12.4	11.7

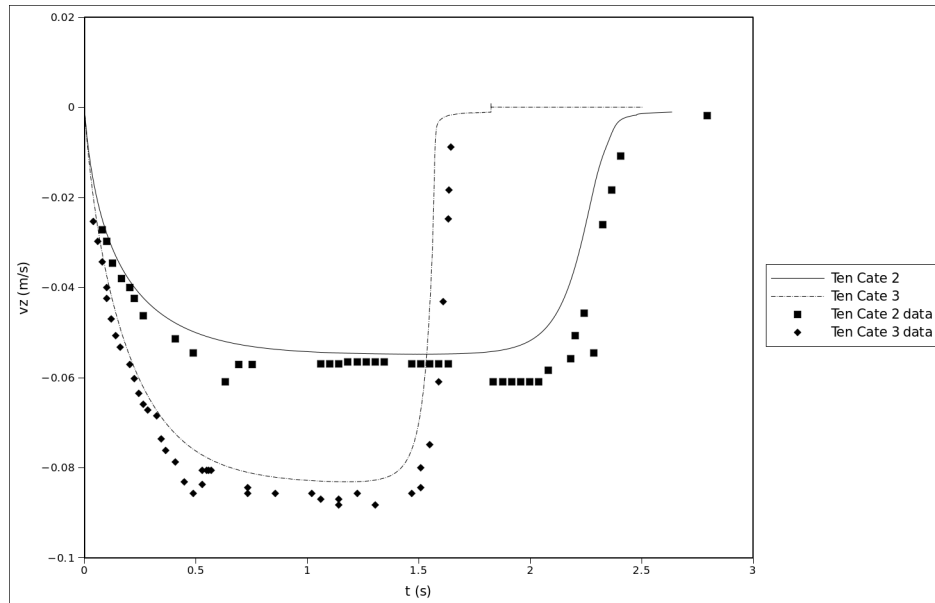


Figure 4.4: Simulations based on the IB method used in this work of experiment cases 2 and 3 in the work of Ten Cate (2002).

Table 4.8: Simulation settings for stationary bubble test

Computational grid	80 x 80 x 80	—
Grid size	0.001	(<i>m</i>)
Numer of time steps	1000	—
Time step	0.0001	(<i>m</i>)
Bubble radius	0.01	(<i>m</i>)
Initial bubble position	(x,y,z) = (0.04,0.04,0.04)	(<i>m</i>)
Liquid density	1000	(<i>kg/m</i> ³)
Liquid viscosity	0.1	(<i>kg/ms</i>)
Gas density	10	(<i>kg/m</i> ³)
Gas viscosity	0.001	(<i>kg/ms</i>)
Surface tension	1	(<i>N/m</i>)

Table 4.9: Stationary bubble test results

Analytical solution	200	(<i>N/m</i> ²)
Numerical solution	200.02	(<i>N/m</i> ²)

4.2 Verification and validation of Front Tracking algorithm

4.2.1 Stationary bubble test

Accuracy of the calculation of the gas-liquid interfacial pressure drop is studied via simulation of a stationary bubble surrounded by a liquid where the gravitational field strength is set to zero. The interfacial pressure drop obtained from simulation is then compared with the Young-Laplace equation:

$$\Delta p = \frac{2\sigma}{R} \quad (4.3)$$

Simulation settings are given in Table 4.8 and the comparison between simulation result and analytical solution is given in Table 4.9. The relative error between analytical solution and simulation results is 0.005 %.

4.2.2 Standard advection test

Gas-liquid interfacial advection and bubble mass conservation is tested by subjecting a bubble to a rotational velocity field flow. Halfway along the simulation the flow field is reversed so as to bring the bubble back to its initial position. The rotational velocity field is given by the following stream function:

$$\psi = \sin^2\left(\frac{y}{b}\right) \sin^2\left(\frac{z}{c}\right) \quad (4.4)$$

Where *b* and *c* represent the size of the domain in the *y*- and *z*-direction

Table 4.10: Simulation settings for standard advection test

Computational grid	80 x 80 x 80	—
Grid size	0.01	(<i>m</i>)
Numer of time steps	1000	—
Time step	0.0001	(<i>m</i>)
Bubble radius	0.15	(<i>m</i>)
Initial bubble position	(x,y,z) = (0.4,0.5,0.4)	(<i>m</i>)
Liquid density	1000	(<i>kg/m</i> ³)
Liquid viscosity	0.1	(<i>kg/ms</i>)
Gas density	10	(<i>kg/m</i> ³)
Gas viscosity	0.001	(<i>kg/ms</i>)
Surface tension	1	(<i>N/m</i>)

Table 4.11: Standard advection error

E1	5.37E-11	%
E2	0.00E+00	%

respectively. The velocity components are given by the following partial derivatives:

$$u_y = -\frac{\partial\psi}{\partial z}, \quad u_z = \frac{\partial\psi}{\partial y}, \quad u_x = 0 \quad (4.5)$$

Simulation settings are given in Table 4.10. Results are given in Figure 4.5 and show that the bubble returns to its initial position and shape. Accuracy is quantified by calculating the error, defined by (Sint Annaland, 2005), for bubble position and shape:

$$E_1 = \frac{\sum_{i,j,k} |F_g^{end}(i,j,k) - F_g^{initial}(i,j,k)|}{\sum_{i,j,k} F_g^{initial}(i,j,k)} \quad (4.6)$$

and for mass conservation:

$$E_2 = \frac{\sum_{i,j,k} F_g^{end}(i,j,k) - \sum_{i,j,k} F_g^{initial}(i,j,k)}{\sum_{i,j,k} F_g^{initial}(i,j,k)} \quad (4.7)$$

Errors for the standard advection test are given in Table 4.11. Results show that mass is conserved to a high degree $O(1E-11)$ and the error between final and initial bubble shape and position is negligible (in fact no error is observed at all).

4.2.3 Oscillating drop

Gas-liquid fluid interaction is taken into account via the addition of a surface tension force term in the Navier-Stokes equation. Correct implementation of the

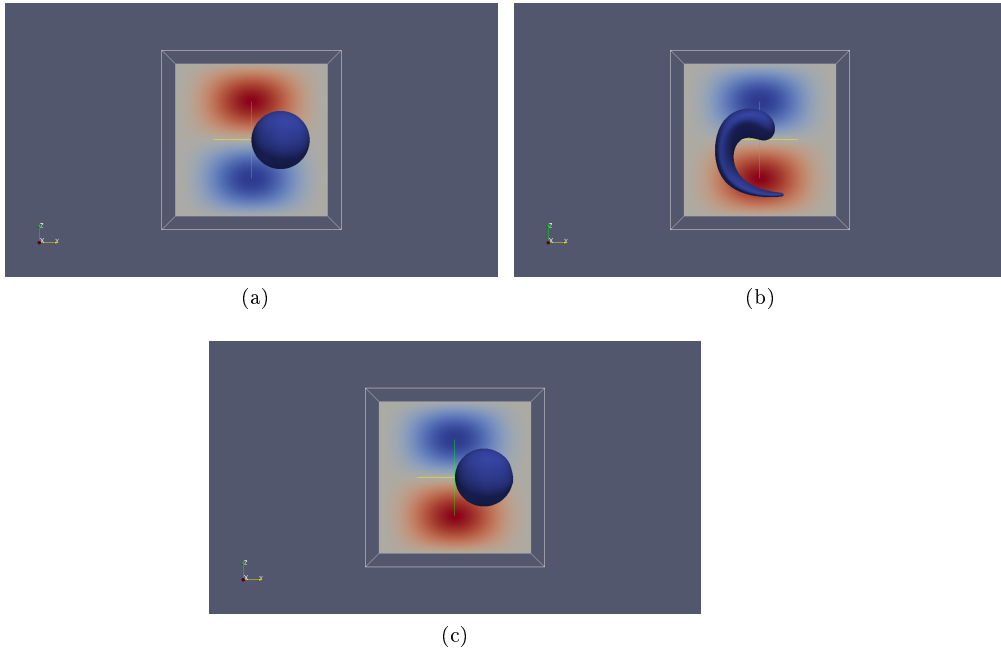


Figure 4.5: Bubble shapes at various times during the standard advection test: (a) initial bubble position and shape at $t = 0$ s, (b) intermediate bubble position and shape at $t = 0.5$ s and (c) final bubble position and shape.

surface tension force is tested via simulation of an oscillating drop surrounded by a gas where gravitational field strength is zero.

The shape of a drop r in spherical coordinates may be represented as (Foote, 1973):

$$d(\theta, t) = d_e + \sum a_n(t) P_n(\cos(\theta)) \quad (4.8)$$

where a_n are coefficients dependent on time t , θ is the polar angle and P_n is the n th order Legendre polynomial. In this work the polar angle is taken to be equal to 0, $\theta = 0$, reducing eq. (4.8) to:

$$d(t) = d_e + \sum a_n(t) \quad (4.9)$$

For potential flow and small distortions in the shape of the drop relative to the shape of the drop at rest the coefficients can be given by:

$$a_n = b_n \cos(\omega t) \quad (4.10)$$

where b_n is some amplitude of the n th mode.

The frequency ω of the oscillation is given by:

$$\omega = \sqrt{\frac{8n(n-1)(n+2)\sigma}{\rho_d d_e^3}} \quad (4.11)$$

Damping of droplet oscillation of droplets with low viscosity in dynamically inactive surroundings has been investigated by (Lamb, 1932), who arrived at the following expression for the gradual damping of the oscillation amplitude:

$$b = b_0 e^{-\beta t} \quad (4.12)$$

where b_0 is the initial amplitude and β is the inverse of the decay rate. The decay rate inverse is given by:

$$\beta = \frac{4(n-1)(2n+1)\mu_d}{\rho_d d_e^2} = \frac{1}{\tau} \quad (4.13)$$

Substituting all relevant equations into equation 4.9 and considering only the fundamental frequency ($n = 2$) gives the following relation for the diameter of the droplet as a function of time:

$$d(t) = d_e + b_0 e^{-\beta t} \cos(\omega t) \quad (4.14)$$

The simulation settings used in this verification test are given in Table 4.12. These settings are the same as those used in Seelen (2012). Simulation results are shown in Figure 4.6 and show good agreement between analytical solution and simulation results.

Table 4.12: Simulation settings used in oscillating drop test

V_b	4.293178	(m^3)
d_e	2.0162	(m)
a_e	0.0338	(m)
ρ_d	100	(kg/m^3)
μ_d	0.35	(kg/ms)
ρ_c	1	(kg/m^3)
μ_c	0.001	(kg/ms)
σ	10	(N/m)
n	2	(-)

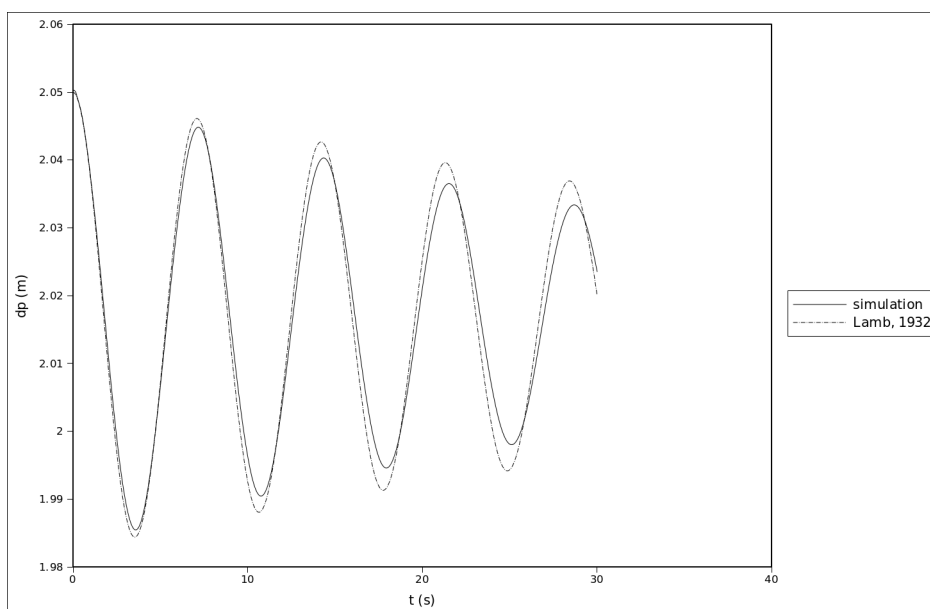


Figure 4.6: Droplet diameter as a function of time.

Table 4.13: Settings for free rise velocity and bubble shape simulations

	A	B	C	D	E
ρ_l (kg/m^3)	600	1000	2000	2000	1000
ρ_g (kg/m^3)	1.21	1.21	1.21	1.21	1.25
μ_l (kg/ms)	0.0845	0.025	0.0501	0.0282	0.001
μ_g (kg/ms)	1.52E-05	1.52E-05	1.52E-05	1.52E-05	1.80E-05
σ (N/m)	0.0940	0.0157	0.00314	0.00314	0.214
d_b (m)	0.004	0.004	0.004	0.004	0.0066
Eu	1	10	100	100	2
M	0.001	0.001	1	0.1	1.00E-12
Computational grid	150 ³	150 ³	150 ³	150 ³	100x100x120
Resolution	15	15	15	15	20

Table 4.14: Comparison of bubble Reynolds number obtained from simulation with Grace diagram

	M	Eu	v_z m/s	Re (simulation)	Re (Grace, 1973)
A	0.001	1	0.081	2.30	1.8
B	0.001	10	0.15	24.08	20
C	1	100	0.12	19.56	18
D	0.1	100	0.13	36.88	35
E	1.00E-12	2	0.36	2376	2000

4.2.4 Free rise velocity and bubble shape

Performance of the front tracking method in predicting actual flows is evaluated by carrying out a set of simulations of single bubbles rising in an initially quiescent liquid. Rise velocities and bubble shapes obtained from simulation are compared with experimental data. Experimental data on bubble rise velocities and shape are summarized in the diagram constructed by Grace (Grace, 1973). A comparison of predicted bubble Reynolds numbers with Reynolds numbers given by the diagram of Grace (1973) is given in Table 4.14. Rise velocities and bubble shapes are predicted fairly well by the front tracking method.

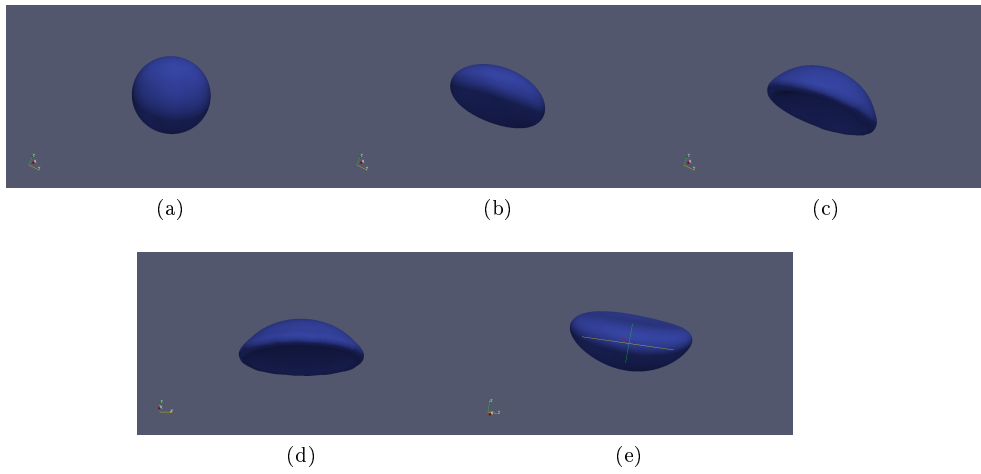


Figure 4.7: Shapes of bubbles observed in single free rising bubble simulations. (a) Bubble shape observed in case A. (b) Bubble shape observed in case B. (c) Bubble shape observed in case C. (d) Bubble shape observed in case D. (e) Bubble shape observed in case E.

Chapter 5

Particle-laden and bubbly flows

5.1 Particle-laden flows

Simulations of particle-laden flows have been performed to study the effect of particle density and solids fraction on the drag force exerted on the particles by the liquid. Particles are placed in random locations using a Monte Carlo algorithm in a, initially quiescent, liquid filled cubic box with periodic boundaries. A snapshot of a typical particle-laden flow simulation is shown in Figure 5.1. It shows the three dimensional simulation domain filled with particles. The plane intersecting the domain displays the local z-component of the velocity field. In this particular simulation the density of the solids is lower than that of the surrounding liquid, consequently the particles flow upwards. Note the z-component of the local velocity of the liquid adjacent to the particle surface is positive around rising particles, consistent with the no-slip condition imposed at the solid-liquid interface.

Simulations are compared with predictions based on correlations derived by Beetstra (2007) and Tang (2014). Beetstra (2007) performed lattice Boltzmann simulations of fluids flowing around a monodisperse random array of spheres. The data obtained from these simulations (Beetstra, 2007) was used deduce a correlation for the stokes normalized drag force as a function of the solids fraction and particle Reynolds number:

$$F = \frac{10\frac{\phi}{(1-\phi)^2} + (1-\phi)^2(1+1.5\sqrt{\phi}) + \frac{0.413Re}{24(1-\phi)^2} \left[\frac{(1-\phi)^{-1} + 3\phi(1-\phi) + 8.4Re^{-0.343}}{1 + 10^3\phi Re^{-(1+4\phi)/2}} \right]}{(5.1)}$$

with ϕ the solids fraction and F the stokes normalized dimensionless drag force defined as:

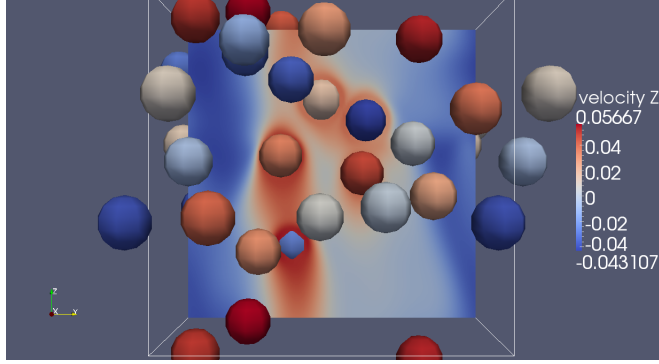


Figure 5.1: Snapshot of simulation Case 1. The z-component of the velocity field is displayed on the cross section plane.

$$F = \frac{|\mathbf{F}_D|}{3\pi\mu d|\mathbf{U}|} \quad (5.2)$$

where \mathbf{F}_D is the drag force (N) and \mathbf{U} the superficial slip velocity (m/s), defined as $\mathbf{U} = (1 - \phi)(\mathbf{v} - \mathbf{u})$. The Reynolds number is defined as $Re = \frac{\rho_f d_p |\mathbf{U}|}{\mu_l}$. In calculations performed in this work for determining the dimensionless drag force the buoyancy and gravitational forces are taken to be equal to the drag force, which is a valid approximation when the system has reached a time invariant state. The average solids velocity $\langle \mathbf{v} \rangle$:

$$\langle \mathbf{v} \rangle = \frac{\sum_{i,j,k} \mathbf{u} \alpha_{i,j,k} h^3}{\sum_{i,j,k} \alpha_{i,j,k} h^3} \quad (5.3)$$

and the average liquid velocity:

$$\langle \mathbf{u} \rangle = \frac{\sum_{i,j,k} \mathbf{u} (1 - \alpha_{i,j,k}) h^3}{\sum_{i,j,k} (1 - \alpha_{i,j,k}) h^3} \quad (5.4)$$

required for calculating the superficial velocity \mathbf{U} , are calculated at each time step. The average solids and liquid velocities are time averaged over the simulation time t_f , excluding the initial transient period of around 0.1 s.

Tang (2014) performed simulations of fluids flowing around monodisperse random array of spheres using an immersed boundary method following Kriebitzsch (2011). The data was used to derive two drag force correlations for the stokes normalized drag force, one for Reynolds 50 and another for Reynolds 100, as a function of the solids fraction. For Reynolds 50 Tang (2014) proposed:

Table 5.1: Simulation settings for particulate flows

	1	2	3	4	5	6	7	8
Nx	121	121	121	121	121	139	129	115
dx	5e-5	5e-5	5e-5	5e-5	5e-5	5e-5	5e-5	5e-5
$\mu_l (kg/ms)$	0.001	0.001	0.001	0.001	0.001	0.001	0.001	0.001
$\rho_l (kg/m^3)$	1000	1000	1000	1000	1000	1000	1000	1000
$\rho_s (kg/m^3)$	700	1000	1300	1600	1900	2000	2000	2000
N_p	32	32	32	32	32	48	38	27
$d_p (m)$	0.001	0.001	0.001	0.001	0.001	0.001	0.001	0.001
$t_f (s)$	1	1	1	0.85	0.8	0.23	0.32	0.52

$$F = \frac{1}{(1 - \phi)^3 \left(0.4765 - 0.2694\phi^{\frac{1}{3}} - 0.641\sqrt{\phi} + 0.9255\phi - 0.5904\phi^2 \right)} \quad (5.5)$$

and for Reynolds 100:

$$F = \frac{1}{(1 - \phi)^3 \left(0.2829 + 1.6162\phi^{\frac{1}{3}} - 3.3701\sqrt{\phi} + 2.4318\phi - 1.1539\phi^2 \right)} \quad (5.6)$$

A total of 16 simulations have been performed of flows with particles of various densities and at various solids fractions. Simulation settings are given in Tables 5.1 and 5.2. The dimensionless drag force and corresponding Reynolds number, calculated from simulation data and correlations, of each simulation case is given in Tables 5.3 and 5.4. The effect of particle density on drag force exerted on particles is studied in cases 1 - 5. In these cases simulations are performed of systems with 32 particles, with densities ranging from 700 to 1900 kg/m^3 . A plot of the average z-component of the average solids velocity as a function of time for cases 1 - 5 is shown in Figure 5.2. In case 1 and 3 the difference between the particle and liquid densities are equal in magnitude, but opposite in sign. Therefore the terminal rise velocity of the particles in case 1 is expected to be equal in magnitude, but opposite in sign relative to the terminal sedimentation velocity of particles in case 3. Results show the particle velocities are close in value, with the average particle sedimentation velocity of particles in case 3 is 16 % lower than the rise velocity of particles in case 1. The rest of the cases, 3 - 5, show that as the density increases, so does the particle Reynolds number due to the increase in gravitational force relative to the buoyancy force.

A discontinuity is present in the average sedimentation velocities of cases 3 and 4. The discontinuity corresponds to the time the simulation was restarted (the allowed run time on the computer cluster on which simulations are carried out was limited to one month for these particular simulations). Simulations are restarted using data which is periodically stored in dump files as the simulations are running. Prior to the implementation of the numerical scheme for calculating

Table 5.2: Simulation settings for particulate flows

	9	10	11	12	13	14	15	16
Nx	110	121	121	121	121	121	121	121
dx	5e-5	5e-5	5e-5	5e-5	5e-5	5e-5	5e-5	5e-5
$\mu_l (kg/ms)$	0.001	0.001	0.001	0.001	0.001	0.001	0.001	0.001
$\rho_l (kg/m^3)$	1000	1000	1000	1000	1000	1000	1000	1000
$\rho_s (kg/m^3)$	2000	2000	2000	2000	2000	2000	2000	2000
N_p	24	11	21	43	43	53	64	75
$d_p (m)$	0.001	0.001	0.001	5e-4	0.001	0.001	0.001	0.001
$t_f (s)$	0.53	0.46	0.403	0.45	0.22	0.28	0.26	0.24

Table 5.3: Simulation results for particulate flows

	1	2	3	4	5	6	7	8
ϕ	0.076	0.076	0.076	0.076	0.076	0.075	0.074	0.074
ϕ_E	0.10	0.10	0.10	0.10	0.10	0.10	0.10	0.10
<i>Re</i> Simulation	36	0	30	47	58	70	65	66
F	4.9	-	5.9	7.5	9.1	8.4	9.1	8.9
<i>Re</i> Beetstra (2007)	39	0	39	60	78	83	83	83
F	4.2	1.8	4.2	5.4	6.3	6.5	6.5	6.5
<i>Re</i> Beetstra (2007), ϕ_E	36	0	36	56	73	78	78	78
F	4.6	1.8	4.6	5.8	6.8	7.0	7.0	7.0
<i>Re</i> Tang (2014), <i>Re</i> = 50	50	50	50	50	50	50	50	50
F	5.0	5.0	5.0	5.0	5.0	5.0	5.0	5.0
<i>Re</i> Tang (2014), <i>Re</i> = 100	100	100	100	100	100	100	100	100
F	5.8	5.8	5.8	5.8	5.8	5.8	5.8	5.8

Table 5.4: Simulation results for particulate flows

	9	10	11	12	13	14	15	16
ϕ	0.076	0.026	0.050	0.013	0.10	0.125	0.15	0.18
ϕ_E	0.10	0.035	0.066	0.022	0.14	0.17	0.2	0.24
<i>Re</i> Simulation	67	96	78	24	60	50	47	40
F	8.8	5.8	7.4	2.9	10.1	12.6	13.7	16.6
<i>Re</i> Beetstra (2007)	83	95	89	26	77	72	67	63
F	6.6	5.7	6.1	2.6	7.0	7.5	8.1	8.7
<i>Re</i> Beetstra (2007), ϕ_E	78	93	85	26	70	64	58	53
F	7.0	5.9	6.4	2.6	7.7	8.5	9.3	10.3
<i>Re</i> Tang (2014), <i>Re</i> = 50	50	50	50	50	50	50	50	50
F	5.0	3.4	4.2	2.9	5.9	6.7	7.8	8.9
<i>Re</i> Tang (2014), <i>Re</i> = 100	100	100	100	100	100	100	100	100
F	5.8	3.9	4.8	3.3	7.0	8.1	9.4	10.8

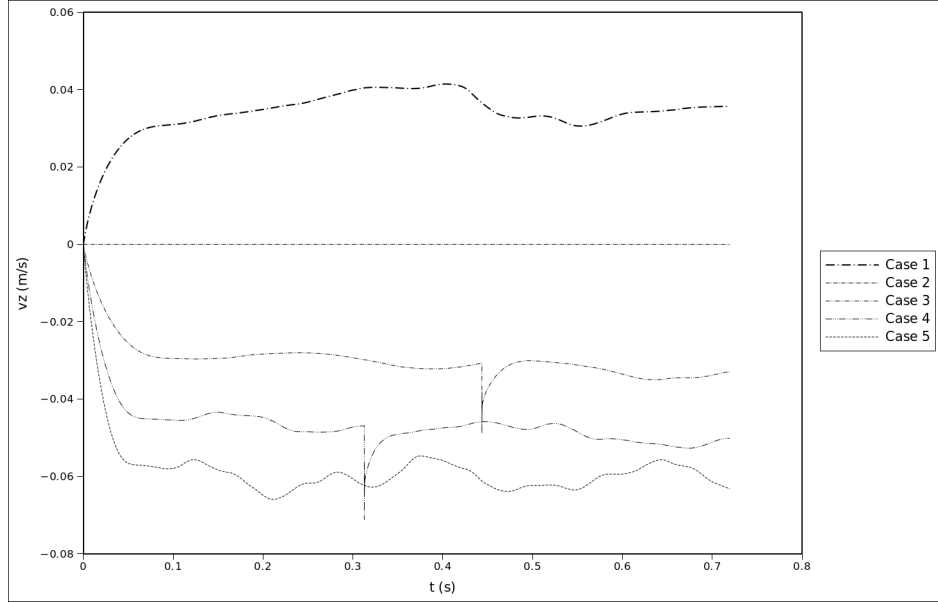


Figure 5.2: Average sedimentation velocities at various densities

particle momenta, all data required for restarting simulations (velocity fields, pressure fields, etc) was stored in the dump files. However the velocity fields at the previous time step, required in the numerical scheme for calculating particle momenta (see equation 2.25), was not stored in the dump files. This resulted in a sudden increase in particle velocity. In light of the issue velocity fields at previous time steps are now also stored in dump files, which solved the issue. The actual physical effects of this computer code error is that an impulse of force is exerted on the particles. The force only lasts for one time step, after which the effects gradually dissipate and the average particle velocity returns to its terminal velocity.

A plot of the dimensionless drag force calculated from simulation data and correlations of Beetstra (2007) and Tang (2014) against the Reynolds number is shown in Figure 5.3. The correlation of Beetstra (2007) predicts lower drag forces at a given Reynolds number in comparison with simulations. The increased drag observed in simulations may be attributed to the enlargement of particle diameter associated with the use of distribution functions in the IB method used in this work. However, from purely physical arguments, the increased drag cannot entirely be attributed to the effects of distribution functions. The higher drag observed in simulations performed in this work must also be a consequence of the fact that the correlations of Beetstra (2007) are being based on simulations of fluids flowing around fixed particles. Particles which move freely through the liquid are influenced by the wakes of other particles resulting in nonvertical motion, particle collisions and particle rotation which enhances

particle drag.

A rough estimate of the effect of particle enlargement, which is in the order of the size of a grid cell, on drag force can be obtained by calculating the dimensionless force using Beetstra (2007) based on the increased solids fraction ϕ_E and comparing it with the force obtained based on the actual solids fraction of the system. The dimensionless force calculated based on the increased solids fraction is given in Figure 5.3. Comparison with the force calculated based on the actual fraction shows that drag force does indeed increase, but only slightly. It therefore seems that the increased drag observed in simulations can, at most, only partly be attributed to particle enlargement. The increased drag observed in simulations in comparison with the predictions based on correlations is therefore most likely attributed to the increased drag associated with freely moving particles.

The correlation of Tang (2014) for Reynolds 50 and 100 predict similar drag forces as observed in simulation for cases 1 and 3, but lower drag forces for cases 4 and 5. Correlations derived by Tang (2014) were also based on simulations of fixed particles. The increased drag associated with particle mobility therefore not included in these correlations. Systems with moving particles at Reynolds 50 would experience a greater drag force than a corresponding system of fixed particles at the same Reynolds number. Consequently the correlations of Tang (2014) will predict lower drag forces than observed in simulations. The Reynolds 50 correlation of Tang (2014) agrees well with the correlation of Beetstra at Reynolds 50, however the Reynolds 100 correlation predicts a significantly lower drag than Beetstra (2014).

The effect of the solids fraction and particle size on drag force is studied in cases 10 - 16. Here simulations are performed with varying amounts of particles, ranging from 11 to 75, while holding the domain size and particle density constant. The particle size is kept constant in all cases except case 12 where a smaller particle diameter is taken.

Results show that the normalized force increases with solids fraction due to increased effects of confinement. Comparison of the Reynolds numbers calculated from simulation data with Reynolds numbers predicted using correlations shows that Reynolds numbers predicted by correlations are consistently higher, aside from cases 10 and 12, continuing the trend observed in cases 1 - 5. Comparing Beetstra (2007) with simulations shows that the difference between Beetstra (2007) and simulations increases with the solids fraction. The difference diminishes at a solids fraction of approximately $\phi = 0.03$ where it seems agreement between Beetstra (2007) and simulations improves. Correlations of Tang (2014) underestimate drag in all cases but 12, the low Reynolds case.

In case 12 a smaller particle diameter is taken. The settings of case 12 are the same as those of case 13 except for the particle diameter which is reduced by 50 %, relative to the norm used in the other cases (0.001 m), to 0.0005 m. Comparing the simulation results of case 13 with case 12 shows that a reduction in particle size results in a reduction in particle Reynolds number and terminal velocity. Although the reduction in size which results in a lower solids fraction and a reduced effect of the presence of other particles on drag, the reduction in

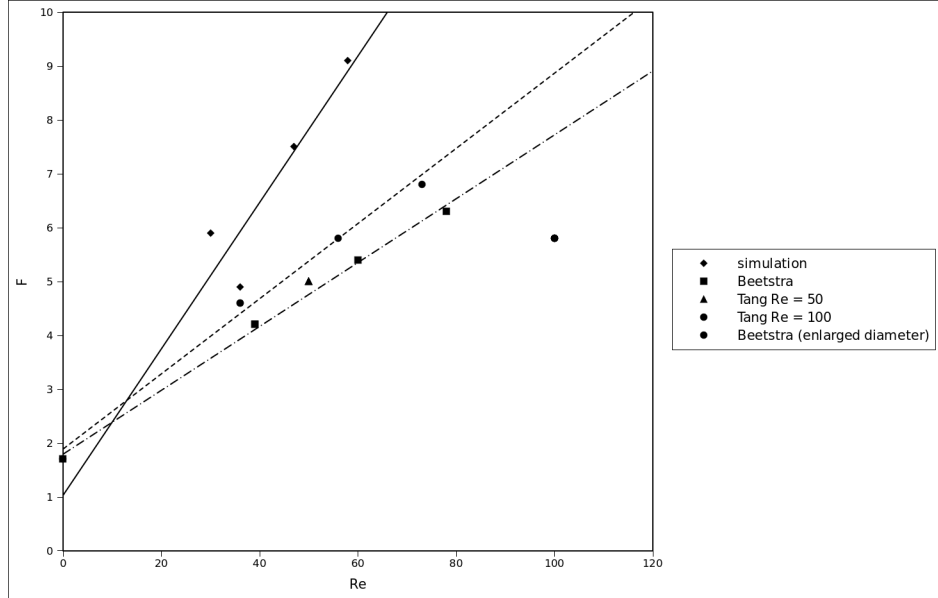


Figure 5.3: Dimensionless force F as a function of the Reynolds number for various particle densities (cases 1 - 5) at $\phi = 0.0756$.

drag associated with a reduction in solids fraction is offset by the increase in particle area to particle weight which increases drag per unit particle weight. A comparison with the correlations of Tang (2014) for Reynolds 50 and 100 shows that both overestimate drag in this low Reynolds case. In contrast the correlation of Beetstra (2007) underestimates drag in this case, although the difference with simulation results is relatively low (8 %).

Aside from determining the effects of parameters on drag force, simulations have also been performed to confirm that a sufficient number of particles have been used in simulations to suppress the effects of periodic boundaries on simulation results. A set of four simulations have been performed, cases 6 - 9, at a solids fraction of 0.0756 with varying amounts of particles, ranging from 24 to 48. A plot of the calculated Reynolds number as a function of the amount of particles is shown in Figure 5.4. The Reynolds numbers obtained from these simulation cases are compared with Reynolds numbers predicted using correlations. Observed Reynolds is practically independent of the amount of particles used these cases, which covers the range of particle numbers used in simulations, apart from cases 10 and 11.

5.2 Bubble flows

Simulations of bubble flows have been performed to study the effect of surface mobility on the drag force exerted on the particles by the liquid. Bubbles

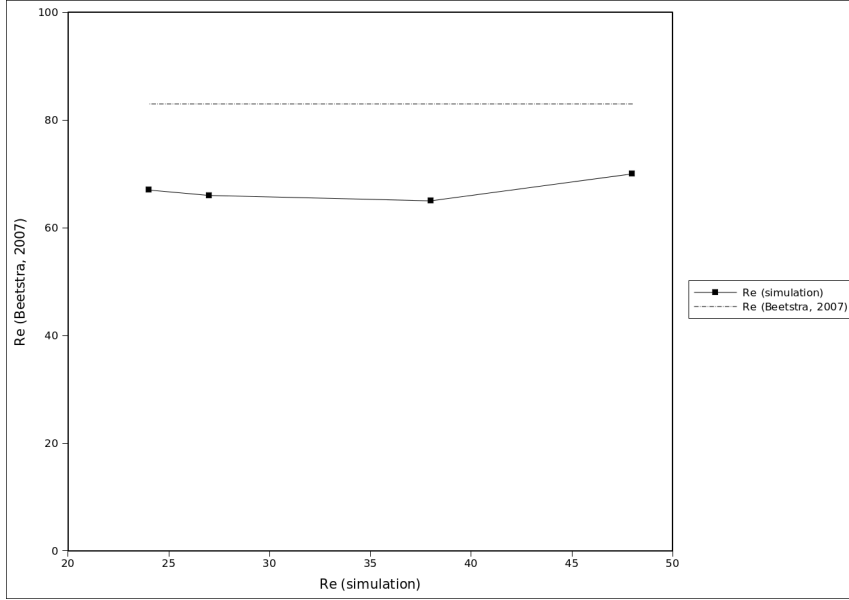


Figure 5.4: Independency of the number of particles

(particles with mobile surfaces) are placed in random locations using a Monte Carlo algorithm in a, initially quiescent, liquid filled cubic box with periodic boundaries as was done in the particle-laden simulations.

Surface mobility is expected to reduce drag. Hadamard (1911) compared the drag force exerted on single spheres with rigid surfaces with those with mobile surfaces and found that spheres with mobile surfaces experiences two-thirds the drag of a rigid sphere. Surface mobility reduces velocity gradients at the gas-liquid interface reducing viscous stresses at the interface. Although the drag on individual spheres with rigid and mobile surfaces has been studied extensively, less is known about the effect of surface mobility on the flow of a collection of spheres. Several simulations of bubble flows have been compared with the particle laden flow simulations which have been performed. The bubble flow simulation settings are identical to the settings of the corresponding particle-laden flow simulation with which the bubble simulation will be compared. The only difference is surface mobility of the bubbles, which will be varied by varying the surface tension.

Simulations will be compared with predictions based on Results obtained from simulation are compared with the experimentally derived correlations of Tomiyama (1998) for pure liquids:

$$C_{D\infty} = \max \left[\min \left[\frac{16}{Re} (1 + 0.15Re^{0.687}), \frac{48}{Re} \right], \frac{8}{3} \frac{Eo}{Eo + 4} \right] \quad (5.7)$$

and for contaminated liquids:

$$C_{D\infty} = \max \left[\frac{24}{Re} (1 + 0.15 Re^{0.687}), \frac{8}{3} \frac{Eo}{Eo + 4} \right] \quad (5.8)$$

and also with the correlation of Roghair (2012):

$$\frac{C_D}{(1 - \alpha) C_{D\infty}} = 1 + \frac{22}{Eo + 0.4} \alpha \quad (5.9)$$

obtained from simulations of bubble flows using a front tracking method. In the correlation of Roghair (2012) the drag force coefficient for single bubbles is given by the correlation proposed by Dijkhuizen (2008):

$$C_{D\infty} = \sqrt{C_D (Re)^2 + C_D (Eo)} \quad (5.10)$$

where the Reynolds part is given by the correlation of Mei (1994) and the Eotvos term given by a correlation proposed in Dijkhuizen (2008).

A total of 9 simulations of bubble flows have been performed. Simulation settings are given in Table 5.5 and 5.6. Corresponding results are given in Tables 5.7 and 5.8. Effect of surface mobility is studied in the first four cases of the bubble flow simulations, cases 1 - 4. Results of these are compared with case 1 of the particle-laden flow simulations. The settings of these cases are identical to the settings of case 1 of the particle-laden flow simulations, except for the fact that the gas-liquid interface is mobile. Mobility of the surface is varied by varying the interfacial tension σ thereby varying the Eotvos number ($Eo = \frac{g_z d_b^2 \rho_l}{\sigma}$). Increased surface tension reduces mobility, and increases drag.

Comparison of the average bubble rise velocity observed in cases 1 - 4 of the bubble flow simulations with case 1 of the corresponding particulate flow simulation shows that the particle Reynolds numbers are indeed lower than the bubble Reynolds numbers observed in cases 1 - 4. Bubbles experience a reduced drag in comparison with particles with rigid surfaces. With the drag force coefficient proportional to the inverse of the square of the Reynolds number the ratio of the drag force coefficient of the particle to the drag force coefficient of the bubble is:

$$\frac{C_{D,b}}{C_{D,p}} = \frac{Re_p^2}{Re_b^2} \quad (5.11)$$

Taking the ratio of the square of the average bubble Reynolds numbers of cases 1 - 4 of the bubbly flow simulations to the square of the average particle Reynolds number of case 1 of the particle-laden flow simulations gives a value of 0.36. This ratio is smaller than the 2/3 ratio observed for single particles. The increase in drag exerted on rigid particles due to the presence of other particles is greater than the increase in drag exerted on particles with rigid surfaces in the presence of other particles with mobile surfaces.

As surface mobility decreases the drag force should increase, and this is indeed observed in simulation results. Comparison of case 3 and 4 shows the

Table 5.5: Simulation settings and results for bubbly flows

	1	2	3	4	5	6
Nx	121	121	121	121	121	121
dx (m)	5e-5	5e-5	5e-5	5e-5	2.5e-5	2.5e-5
μ_l (kg/ms)	0.001	0.001	0.001	0.001	0.001	0.001
ρ_l (kg/m ³)	1000	1000	1000	1000	1000	1000
μ_g (kg/ms)	1.8e-5	1.8e-5	1.8e-5	1.8e-5	1.8e-5	1.8e-5
ρ_g (kg/m ³)	700	700	700	700	700	700
σ_s (N/m)	0.073	0.04905	0.0981	0.0245	0.073	0.012263
d_b (m)	0.001	0.001	0.001	0.001	0.0005	0.0005
Eo	0.134	0.2	0.1	0.4	0.0335	0.2
$\log(Mo)$	-11.12	-10.6	-11.51	-9.70	-11.12	-8.80
t_f (s)	1.0	1.0	1.0	1.0	1.0	1.0

higher Reynolds number is observed in case 4, where a smaller value was taken for the surface tension.

In cases 5 and 6 the bubble diameter is reduced by 50 %, to 0.0005 m, relative to the value used in cases 1 - 4. A reduced bubble Reynolds number is observed associated with the reduction in bubble diameter, due to increase in area per unit bubble volume which enhances bubble drag. A reduction in Reynolds number was also observed in the particle-laden cases when the diameter of the particle was reduced, holding the remaining parameters constant. In case 7 the diameter is doubled to 0.002 m and a corresponding increase in Reynolds number is observed.

The density of the gaseous phase is varied in cases 8 and 9. Results show a decrease in the buoyancy driving force, $\Delta\rho$, results in a decrease in Reynolds numbers.

Comparison with predictions based on correlations shows that predictions based on the correlation of Tomiyama (1998) for single bubbles in contaminated liquids was the correlation which was in greatest agreement, within 15 %, with simulations. The correlation for pure liquids underestimated drag in all cases. Gas-liquid interfaces are more mobile in pure liquids than contaminated ones, resulting in decreased drag. The correlation proposed by Roghair (2012) predicted higher drag forces than observed in simulations, apart from case 7. However this correlation was derived in the wobbling region (Grace, 1973) for the region $1 < Eo < 5$ and overestimates drag at lower Eotvos numbers (Ivo, 2012). Predictions based on the correlation proposed by Beetstra (2007) for rigid particles have also been made. These consistently overestimate drag, as expected since the no-slip condition at rigid particle surfaces increases drag.

Table 5.6: Simulation settings for bubbly flows

	7	8	9
Nx	121	121	121
dx (m)	1e-4	5e-5	5e-5
μ_l (kg/ms)	0.001	0.001	0.001
ρ_l (kg/m ³)	1000	1000	1000
μ_g (kg/ms)	1.8e-5	1.8e-5	1.8e-5
ρ_g (kg/m ³)	700	500	900
σ_s (N/m)	0.0613125	0.04905	0.04905
d_b (m)	0.002	0.001	0.001
Eu	0.64	0.2	0.2
$\log(Mo)$	-10.89	-10.38	-11.08
t_f (s)	1.0	1.0	1.0

Table 5.7: Simulation results for bubbly flows

	1	2	3	4	5	6
α	0.0756	0.0756	0.0756	0.0756	0.0756	0.0756
Eu	0.134	0.2	0.1	0.4	0.0335	0.2
Re (Simulation)	51	53	52	55	13	13
Re (Case 1 particle flows)	36	36	36	36	-	-
Re Tomiyama (1998) cont.	51	51	51	51	11	12
Re Tomiyama (1998) pure	81	82	81	82	15	15
Re Roghair	33	35	31	41	5	6
Re Beetstra	33	33	33	33	8	8

Table 5.8: Simulation results for bubbly flows

	7	8	9
α	0.0756	0.0756	0.0756
Eu	0.64	0.2	0.2
Re (Simulation)	175	62	25
Re Tomiyama (1998) cont.	196	71	24
Re Tomiyama (1998) pure	292	136	31
Re Ivo	201	54	14
Re Beetstra	111	46	16

Chapter 6

Conclusion

A new numerical scheme for calculating particle momenta has been implemented in the immersed boundary scheme developed by (Kriebitzsch, 2010). The new IB method has been validated by comparing simulation results with predictions based on correlations derived from experiment or other simulations. Results obtained with the new IB method were compared with the previous IB method, which followed Kriebitzsch (2010). The error between the two methods was within 1 %.

Simulations were performed of single particles rising and settling in liquids. The results were compared with predictions based on correlations of Turton and Levenspiel (1986) and Beetstra (2007) and found to generally agree within 8 %. Simulations of single settling particles were also compared with the experimental work of Mordant (2000) and Ten Cate (2002). Comparison showed that simulations agree well with the experimental work, within 8 %. The settling velocities observed in simulations was slightly lower than that observed in the work done by Mordant (2007) and Ten Cate (2002). This could be attributed to confinement effects, which is a plausible explanation for the reduced velocity observed in the simulation results representing an experimental case in Mordant (2000), due to the difference in domain size to particle size ratio between the experimental set up and simulation settings. However the simulation settings used in representing the experiments performed in Ten Cate (2002) match the experimental conditions exactly (domain size, particle size, etc). Therefore the reduced velocity is not likely to be attributable to confinement effects, but rather to an increased effective diameter resulting from the use of distribution functions to interpolate quantities to and from the Eulerian and Lagrangian grids. Although it has been assumed that particle resolutions used in this work was sufficient, an assumption based on preliminary simulations and the work of Kriebitzsch (2011) it cannot be ruled out that that results were entirely resolution free.

Particle-laden flow simulations have been performed to study the effect of particle density and solids fraction on particle drag. Results show that for the cases studied in this work, the drag force at a given solids fraction was roughly

proportional with the particle Reynolds number. When the solids fraction is varied, holding other parameters constant, an increase in drag with solids fraction is observed due to confinement effects.

The particle-laden flow simulations were compared with predictions based on the correlations of Tang (2014) and Beetstra (2007). In nearly all cases the correlations of Tang (2014) and Beetstra (2007) predicted lower drag forces than observed in simulations. This is attributable to two things. The first is the wakes of particles affect the motion of other particles, resulting in nonvertical particle motion and rotation which enhances particle drag. The second is that the diameter of the particles is enlarged by the use of distribution functions (Tang, 2014). However it has been shown, based on calculations at different solids fractions using the correlation of Beetstra (2007), that the increase in particle diameter cannot account for the increase in drag observed in simulations. Consequently, it is likely that the increased drag observed in simulations is a consequence of enhanced particle-particle interaction in systems with freely moving particles.

Bubble simulations have also been performed, using a front tracking (FT) method, to study the effects of surface mobility on drag. Single bubbles rising in an initially quiescent liquid were simulated and compared with the diagram of Grace (1973). The comparison showed that simulations predicted bubble shape and rise velocity reasonably well. Simulations of swarms of bubbles were performed at various Eotvos ($Eo < 1$) and compared with a particle-laden simulation. Comparison showed that the ratio of the drag coefficient of bubbles to the drag coefficient of the particles is 0.36 for the cases studied. A greater force is exerted on an individual rigid sphere by the liquid when the rigid sphere is surrounded by other rigid spheres than on an individual mobile surface sphere by the liquid when the mobile surfaced sphere is surrounded by other spheres with mobile surfaces.

Comparison of bubble simulations with correlations of Tomiyama (1998), Roghair (2012) and Beetstra (2007) showed that the correlation of Tomiyama (1998) for single spheres in contaminated liquids was the correlation agreed the greatest with simulations. The correlation of Roghair (2012) overestimated drag at the low Eotvos numbers taken in the simulation cases. The correlation of Beetstra (2007) also overestimated drag, but this was expected as this correlation is derived for rigid spheres, which experience greater drag.

Chapter 7

Recommendations

Recommendations are presented in summary fashion:

- Perform simulations studying the effect of particle resolution on simulations results to confirm simulations were performed at adequate resolutions.
- Determine whether the IB method used in this work suffers from the effects of an enlarged diameter associated with the use of distribution functions. If so introduce the implicit fluid-solid coupling outlined by Deen (2012).

Bibliography

- [1] D. Darmana, N.G. Deen, J.A.M. Kuipers. Detailed modeling of hydrodynamics, mass transfer and chemical reactions in a bubble column using a discrete bubble model. *Chemical Engineering Science*, 60(12): 3383–3404, 2005.
- [2] D. Darmana, R.L.B. Henket, N.G. Deen, J.A.M. Kuipers. Detailed modelling of hydrodynamics, mass transfer and chemical reactions in a bubble column using a discrete bubble model: Chemisorption of CO₂ into NaOH solution, numerical and experimental study. *Chemical Engineering Science*, 62(9): 2556–2575, 2007.
- [3] N.G. Deen, M. van Sint Annaland and J.A.M. Kuipers. Multi-scale modeling of dispersed gas-liquid two-phase flow. *Chemical Engineering Science*, 59: 1853-1861, 2004.
- [4] N.G. Deen, M. van Sint Annaland and J.A.M. Kuipers. Direct numerical solution of complex multi-fluid flows using a combined front tracking and immersed boundary method. *Chemical Engineering Science*, 64: 2186-2201, 2009.
- [5] N. G. Deen, S. Kriebitzsch, M.A. van der Hoef, J.A.M. Kuipers. Direct numerical simulation of flow and heat transfer in dense fluid–particle systems. *Chemical Engineering Science*, 81: 329–344, 2012.
- [6] J.A.M. Kuipers, W.P.M. van Swaaij. Computational fluid dynamics applied to chemical reaction engineering. *Adv. Chem. Eng.* 24: 227–328, 1998.
- [7] N.G. Deen, R.F. Mudde, J.A.M. Kuipers, P. Zehner and M. Kraume. *Ullmann’s Encyclopedia of Industrial Chemistry*, chapter Bubble Columns, Wiley-VCH Verlag GmbH & Co. KGaA, Weinheim, 2010.
- [8] I. Roghair. Direct numerical simulations of hydrodynamics and mass transfer in dense bubbly flows. PhD thesis, *Technische Universiteit Eindhoven*, 2012.
- [9] L. Seelen. Combining the Front Tracking and Immersed Boundary method. MSc thesis, *Technische Universiteit Eindhoven*, 2012.

- [10] S.O. Unverdi and G. Tryggvason. A Front-Tracking method for viscous, incompressible, multi-fluid flows. *J. Comp. Ph.*, 100: 25-37, 1992.
- [11] M. Uhlmann. An immersed boundary method with direct forcing for the simulation of particulate flows. *J. Comp. Ph.*, 209: 448-476, 2005.
- [12] C.S. Peskin. The immersed boundary method. *Acta Numerica*, 479-517, 2002.
- [13] C.S. Peskin. Flow patters around heart valves: a numerical method. *J. Comp. Ph.*, 10: 252-271, 1972.
- [14] T. Kempe and J. Frohlich. An improved immersed boundary method with direct forcing of the simulation of particle laden flows. *J. Comp. Ph.*, 231: 3663-3684, 2012.
- [15] S. Kriebitzsch. Direct numerical simulation of dense gas-solid flows. PhD thesis, *Technische Universiteit Eindhoven*, 2011.
- [16] A. Prosperetti. Navier-Stokes numerical algorithms for free-surface flow computations: an overview, Drop-surface interaction. 237, 2002.
- [17] W. Dijkhuizen. Derivation of closures for bubbly flows using Direct Numerical Simulations. PhD thesis, *Universiteit Twente*, 2008.
- [18] B.P.B. Hoomans, J.A.M. Kuipers, W.J. Briels and W.P.M van Swaaij. Discrete particle simulations of bubble and slug formation in two-dimensional gas-fluidised beds: A hard-sphere approach. *Chemical Engineering Science*, 51: 99-118, 1996.
- [19] Y. Tang, S. Kriebitzsch, E.A.J.F. Peters, M.A. van der Hoef, J.A.M. Kuipers. A methodology for highly accurate results of direct numerical simulations: Drag force in dense gas-solid flows at intermediate Reynolds number. *International Journal of Multiphase Flow*, 62: 73-86, 2014.
- [20] J. Hadamard. Movement permanent d'une sphere liquide et visqueuse dans un liquide visueux. *Comptes Rendus*, 152: 1735, 1911.